

Cholinergic neurons trigger epithelial Ca^{2+} currents to heal the gut

<https://doi.org/10.1038/s41586-023-06627-y>

Received: 6 August 2020

Accepted: 8 September 2023

Published online: 18 September 2023

 Check for updates

Afroditi Petsakou^{1✉}, Yifang Liu¹, Ying Liu¹, Aram Comjean¹, Yanhui Hu¹ & Norbert Perrimon^{1,2✉}

A fundamental and unresolved question in regenerative biology is how tissues return to homeostasis after injury. Answering this question is essential for understanding the aetiology of chronic disorders such as inflammatory bowel diseases and cancer¹. We used the *Drosophila* midgut² to investigate this and discovered that during regeneration a subpopulation of cholinergic³ neurons triggers Ca^{2+} currents among intestinal epithelial cells, the enterocytes, to promote return to homeostasis. We found that downregulation of the conserved cholinergic enzyme acetylcholinesterase⁴ in the gut epithelium enables acetylcholine from specific Egr⁵ (TNF in mammals)-sensing cholinergic neurons to activate nicotinic receptors in innervated enterocytes. This activation triggers high Ca^{2+} , which spreads in the epithelium through Innexin2–Innexin7 gap junctions⁶, promoting enterocyte maturation followed by reduction of proliferation and inflammation. Disrupting this process causes chronic injury consisting of ion imbalance, Yki (YAP in humans) activation⁷, cell death and increase of inflammatory cytokines reminiscent of inflammatory bowel diseases⁸. Altogether, the conserved cholinergic pathway facilitates epithelial Ca^{2+} currents that heal the intestinal epithelium. Our findings demonstrate nerve- and bioelectric⁹-dependent intestinal regeneration and advance our current understanding of how a tissue returns to homeostasis after injury.

The cholinergic pathway is an ancient conserved pathway used by peripheral neurons to communicate with internal organs³. The two cholinergic receptors, nicotinic and muscarinic, and enzymes modulating acetylcholine (ACh) metabolism, for example, acetylcholinesterase (Ace, known as AChE in humans), are highly conserved and expressed in non-neuronal tissues³. Cholinergic receptors regulate ion transport in the intestinal epithelium, which is vital for water and nutrient absorption¹⁰. Recently, attention has been given to the anti-inflammatory properties of the cholinergic pathway, with reduced ACh responsiveness associated with intestinal diseases¹¹.

The *Drosophila* midgut, equivalent to mammalian small intestine, has been used to identify conserved molecular pathways that trigger inflammation and regeneration in the injured epithelium^{1,12}. The midgut epithelium is single-layered and composed of enterocytes (ECs), large polyploid epithelial cells specialized in absorption; secretory enteroendocrine cells; and progenitor cells^{2,13,14}. The visceral muscle and trachea surround the midgut epithelium, whereas anterior and posterior midgut regions are innervated by enteric neurons². When the epithelium is injured, intestinal stem cells (ISCs) divide rapidly, giving rise to daughter cells (enteroblasts) that differentiate into ECs and enteroendocrine cells². Depending on the injury or infection, a multifaceted interplay of conserved inflammatory and regenerative pathways (for example, EGFR, JAK–STAT, Wnt, BMP, Yki) activates ISC proliferation so that a sufficient progenitor cell (ISC and enteroblast) pool replenishes the epithelium¹⁵. Despite the in-depth understanding of how repair is triggered, it is unclear how these pathways are

dampened once the epithelium transitions to homeostasis. Following specific damage, the BMP pathway has been reported to have dual roles, first promoting proliferation and later ISC quiescence^{16,17}.

Here, we provide evidence for the fundamental role of an epithelial bioelectric mechanism controlled by cholinergic neurons that occurs as the midgut transitions from colitis-like injury to homeostasis—a phase we refer to as recovery. We show that during recovery, ECs become more sensitive to ACh by downregulating *Ace* and upregulating *nicotinic Acetylcholine Receptor β3* (*nAChRβ3*). Also, specific Egr-regulated cholinergic neurons, which we refer to as anti-inflammatory recovery-regulating cholinergic enteric neurons (ARCENs), strengthen the axonal properties of their enteric innervations. We demonstrate that transition to homeostasis relies on the healing functions of nAChR-mediated Ca^{2+} currents among ECs, which spread through Innexin2 (Inx2)–Innexin7 (Inx7) gap junctions and are triggered by local ARCEN–EC cholinergic signalling.

ECs are sensitive to ACh during recovery

To study the *Drosophila* intestinal epithelium while it transitions to homeostasis after injury, we damaged the gut with dextran sodium sulfate (DSS), then returned flies to standard food. DSS induces colitis in mammals⁸ and has been used in *Drosophila* to identify conserved proliferative pathways¹⁵. We fed flies DSS for 4 days (injury) followed by 2 or 4 days of standard food (recovery; Fig. 1a). Gut damage elevated the expression of effector *Drosophila* caspase 1 (Dcp1),

¹Department of Genetics, Harvard Medical School, Boston, MA, USA. ²Howard Hughes Medical Institute, Boston, MA, USA. ✉e-mail: Afroditi_Petsakou@hms.harvard.edu; perrimon@genetics.med.harvard.edu

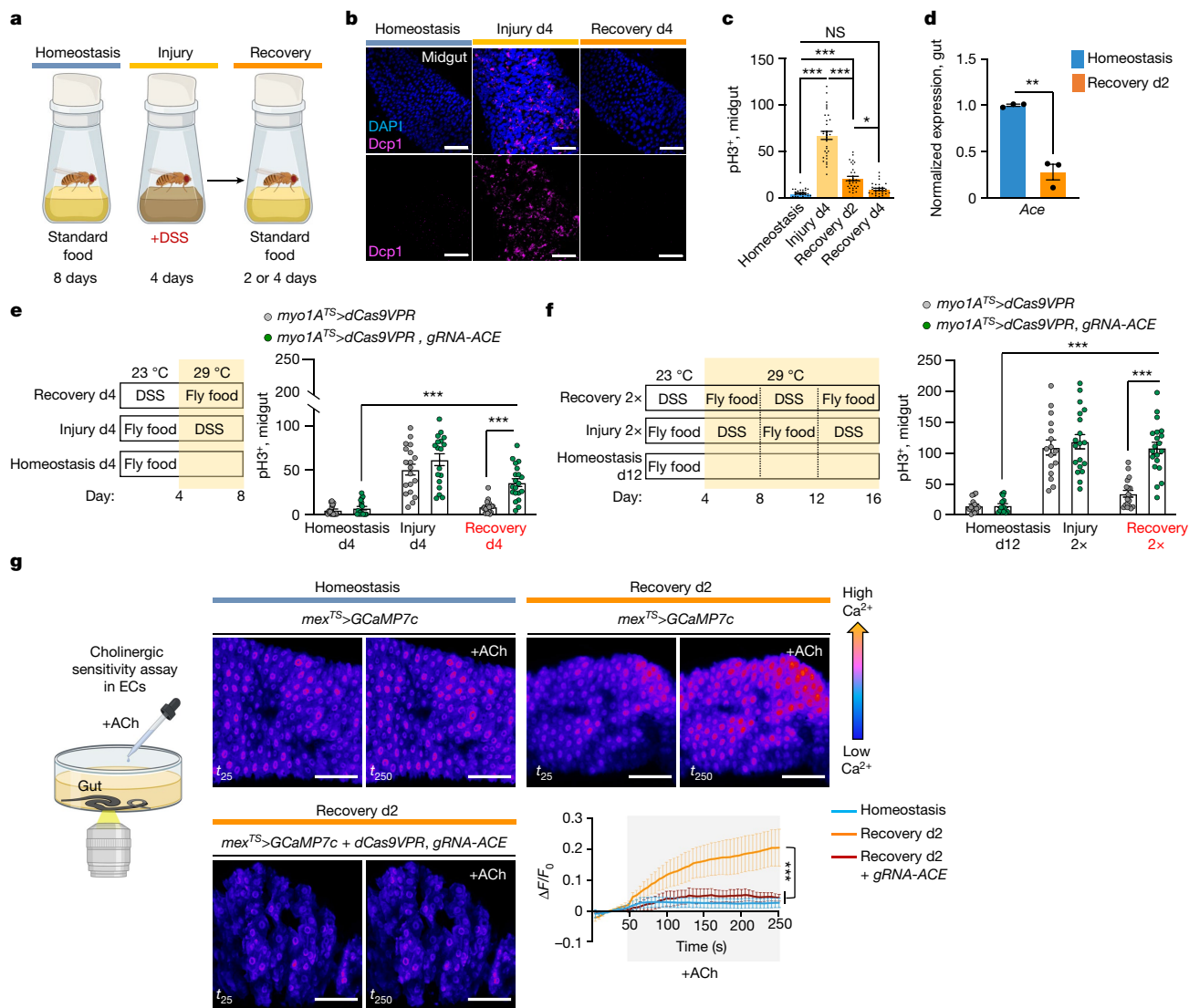


Fig. 1 | ACh sensitivity is required for recovery. **a**, Experimental design illustration. **b**, Midgut of *OreR* flies with cell death marker anti-Dcp1 (magenta) and DAPI (nuclei, blue). Conditions as for **a** at 29 °C. Images are representative of two independent experiments with similar results. Scale bar, 50 μ m. **c**, Mitotic division counts of proliferating ISCs in the midgut of *OreR* flies with anti-pH3 staining (conditions as for **b**). $n = 29 \times$ Dunn's Kruskal–Wallis test: $P = 0.02$ (Recovery day 2 (d2) versus Recovery d4). Black dots indicate counts per gut. NS, not significant. **d**, Expression levels of *Ace* in *OreR* guts. Normalized to Homeostasis. $n = 3$ biologically independent samples per condition (two-tailed t -test, $P = 0.0011$). **e**, Experimental design and graphs of pH3⁺ counts from control flies (*myo1A^{TS}*>*dCas9VPR*) and flies with *Ace* conditionally overexpressed in ECs (*myo1A^{TS}*>*dCas9VPR*, *gRNA-Ace*). Conditional perturbations with temperature-sensitive Gal4 inhibitor, *Tubulin-Gal80^{TS}* (*TS*), allow Gal4 expression at over 27 °C only. Control flies: $n = 18$ (Homeostasis), 19 (Injury), 20 (Recovery) (guts; *gRNA-Ace*: $n = 17$ (Homeostasis), 18 (Injury), 20 (Recovery) guts, from 3 independent experiments. Sidak's and Tukey's two-way analysis of variance

(ANOVA). **f**, Experimental design and graphs of pH3⁺ counts from flies with the same genotypes as in **e**. Control flies: $n = 15$ (Homeostasis d12), 16 (Injury 2 \times), 18 (Recovery 2 \times) guts; *gRNA-Ace*: $n = 14$ (Homeostasis d12), 19 (Injury 2 \times), 20 (Recovery 2 \times) guts, from 3 independent experiments. Sidak's and Tukey's two-way ANOVA. **g**, Assay illustration and colour-coded sequential frames of midgut before (t_{25}) and after (t_{250}) ACh administration of flies conditionally expressing the Ca²⁺ reporter GCAMP7c with the EC driver *mex1-Gal4* (*mex^{TS}*>*GCAMP7c*) and flies overexpressing *Ace* (*mex^{TS}*>*GCAMP7c* + *dCas9VPR*, *gRNA-Ace*; Supplementary Videos 1–3). Recovery: 2 days in standard food (29 °C) after 4 days of DSS feeding (23 °C). Homeostasis: conditions as for Recovery without DSS feeding. Accompanying graph: average relative fluorescence intensity ($\Delta F/F_0$) per frame (5 s per frame) and genotype. $n = 7$ (Homeostasis), $n = 7$ (Recovery d2), $n = 5$ (Recovery d2, *mex^{TS}*>*gRNA-Ace*) guts, from 3 independent experiments. Tukey's two-way ANOVA. Individual $\Delta F/F_0$ values are shown in Extended Data Fig. 2i. Scale bar, 50 μ m. * $0.05 > P > 0.01$, ** $0.01 < P < 0.001$, *** $P < 0.001$. Data are presented as mean \pm s.e.m. Illustrations in **a** and **g** created using BioRender.com.

indicative of cell death (Fig. 1b), and of conserved inflammatory cytokines such as IL-6-like *unpaired 3* (*upd3*)¹⁸ and tumour necrosis factor (TNF) homologue *eiger* (*egr*)⁵ (Extended Data Fig. 1a), resembling DSS-induced colitis⁸. Once flies were transferred to standard food, the epithelium required 4 days to return to homeostasis, as determined by the levels of: (1) inflammatory cytokines (Extended Data Fig. 1a); (2) cell death (Fig. 1b); (3) ISC proliferation (with mitotic marker anti-phospho-Histone3 (pH3); Fig. 1c); and (4) expression of progenitor cell marker *escargot* (*esg*; Extended Data Fig. 1b) and two

markers of mature cells, *pdm1*, marker of ECs, and *prospero* (*pros*), marker of enteroendocrine cells (Extended Data Fig. 1b).

To search for recovery-specific differentially expressed genes, we performed single-nuclei RNA sequencing (RNA-seq) on the second day of recovery (Extended Data Fig. 1c). We identified 14 clusters from 8,073 nuclei recovered, which we assigned to different epithelial cell and progenitor cell populations, as well as to cardia and to cells from the middle region of the midgut (LFC, Cu and Fe regions) (Extended Data Fig. 1c–e). We analysed differential gene expression between

homeostasis and recovery, and observed that *Ace* is highly enriched in ECs and significantly downregulated during recovery (Extended Data Figs. 1f and 2a,b and Supplementary Tables 1 and 2). *Ace* hydrolyses ACh to choline and acetate and thus defines a cell's sensitivity to ACh.

We observed around 75% reduction of *Ace* during recovery (Fig. 1d). Previous intestinal RNA-seq profiling after bacterial infections also detected *Ace* downregulation (Flygut-EPFL data)¹⁹, which we confirmed (Extended Data Fig. 2c). Next, we challenged the gut with injury-inducing chemical bleomycin which triggers different pathways as compared with DSS²⁰. This led to significant *Ace* decrease (Extended Data Fig. 2c), indicating that *Ace* downregulation occurs consistently after different types of intestinal epithelial damage.

To test the role of *Ace* during regeneration, we used CRISPR–Cas9 activation (Extended Data Fig. 2d). We found that 4 days of *Ace* overactivation in ECs (using the Gal4 *myo1A*-driver together with the repressor *Tubulin*-Gal80^{TS}, referred to as *myo1A*^{TS}) led to excessive ISC proliferation during recovery (Fig. 1e), whereas the same activation during homeostasis or injury did not affect proliferation (Fig. 1e). Similarly, consecutive DSS challenges while *Ace* was conditionally overexpressed in ECs using the *myo1A*^{TS} or *mex*^{TS} driver (another EC driver) led to recovery-specific ISC overproliferation (Fig. 1f and Extended Data Fig. 2e). We next tested whether *Ace* perturbations in visceral muscle or immune cells regulated ISC proliferation, and found that they did not (Extended Data Fig. 2f). These findings reveal that overexpressing *Ace* in ECs during recovery prevents ISCs from becoming quiescent, causing an excessive regenerative response. We next tested whether the role of *Ace* during recovery is consistent after different types of epithelial damage. Overexpressing *Ace* in ECs after *Erwinia carotovora* *carotovora* strain 15 (*Ecc15*) infection or bleomycin injury consistently caused overproliferation (Extended Data Fig. 2g,h).

ACh has been proposed to modulate ion transport in the intestinal epithelium in a Ca²⁺-dependent manner¹⁰. Thus, to test for epithelial changes in ACh sensitivity during homeostasis and recovery, we visualized Ca²⁺ by conditionally expressing the Ca²⁺ indicator GCAMP7c (ref. 21) in ECs. Using ex vivo live imaging, we found that Ca²⁺ levels in ECs are significantly higher during recovery following ACh administration than during homeostasis, and that this is attenuated upon overexpression of *Ace* (Fig. 1g, Extended Data Fig. 2i and Supplementary Videos 1–3). These results indicate that during recovery ECs become more sensitive to ACh by decreasing *Ace*, and this change is required for transition to homeostasis after injury.

nAChRβ3 is required in ECs for recovery

Cholinergic receptors are G-protein-coupled muscarinic receptors (mAChR) or ligand-gated ion channel nicotinic receptors (nAChR) made of five homomeric or heteromeric subunits (α1, α2, α3, α4, α5, α6, α7, β1, β2 or β3). To identify which cholinergic receptor becomes activated during recovery, we screened all nAChR subunits and different mAChR subtypes by knocking down their expression in ECs. Conditional knockdown with RNA interference (RNAi) expression targeting *nAChRβ3* in ECs caused overproliferation during recovery (Fig. 2a,b and Extended Data Fig. 3a–c) and after *Ecc15* infection (Extended Data Fig. 3d). Furthermore, *nAChRβ3* knockdown in ECs combined with repeated DSS injury (Recovery 2×) led to hyperplasia (Fig. 2b,c). Conditional knockdown of *nAChRβ3* in ECs significantly reduced the Ca²⁺ response after ACh administration during recovery (Extended Data Fig. 3e,j). Together, these data indicate that reducing *nAChRβ3* in ECs leads to phenotypes resembling *Ace* upregulation. This effect is specific to ECs, as conditionally knocking down *nAChRβ3* in progenitor cells, enteroblasts alone, enteroendocrine cells, visceral muscle or haemocytes had no effect on proliferation (Extended Data Fig. 3f).

The profiling depth of our single-nuclei RNA-seq was not sufficient to conclude whether *nAChRβ3* expression is altered between homeostasis and recovery, despite being solely found in ECs (Extended Data

Fig. 3g). To visualize the expression of nAChRβ3, we inserted a Flag tag within nAChRβ3 (nAChRβ3-flag) (Fig. 2d and Extended Data Fig. 3h). Endogenous nAChRβ3 was significantly enriched in ECs by day 2 of recovery (Fig. 2d), whereas a decrease in *nAChRβ3* levels coincided with return to homeostasis (Extended Data Fig. 3i). nAChRβ3 was localized to the basal side of ECs and some ECs had more nAChRβ3 clustered on their basal side (Fig. 2d,e).

Next, we administered the cholinergic agonist nicotine, which activates nAChRs and cannot be hydrolysed by *Ace*. Nicotine administration significantly increased Ca²⁺ in ECs during recovery compared with homeostasis, reminiscent of ACh sensitivity, and this was diminished when *nAChRβ3* was knocked down (Fig. 2f,g, Extended Data Fig. 3k and Supplementary Videos 4–6). We conclude that *nAChRβ3* in ECs is essential for gut recovery, and recovery-specific enrichment of nAChRβ3 provides a further level of regulation which probably renders ECs more responsive to ACh while the epithelium transitions to homeostasis.

nAChRβ3-mediated Ca²⁺ promotes recovery

ISC proliferation can be triggered by the release of cytokines which vary depending on the stimulus¹⁵. To identify pathways responsible for unrestrained proliferation during recovery after *nAChRβ3* knockdown in ECs, we tested the expression of known cytokines (Fig. 3a and Extended Data Fig. 4a,b). We detected *unpaired 2* (*upd2*) and *upd3* JAK–STAT ligands, together with EGF-like ligand *vein* (*vn*) and *egr*, to be significantly upregulated (Fig. 3a and Extended Data Fig. 4a,b). *Egr* is associated with cell death²², whereas *upd2*, *upd3* and *vn* are upregulated on activation of the Hippo pathway effector Yorkie (*Yki*) in damaged ECs^{23,24}. Supporting this, knocking down *nAChRβ3* in ECs during recovery significantly increased cell death (Extended Data Fig. 4c) as well as expression of *Yki* targets *Diap1* and *Ex* (Extended Data Fig. 4d,e). Also, knockdown of *nAChRβ3* during recovery significantly reduced the transcript and protein levels of *pdm1* (Fig. 3b and Extended Data Fig. 4f,g), whereas *pros* remained unchanged (Extended Data Fig. 4h). These data indicate that disruption of nAChRs in ECs during recovery impairs ECs, leading to cell death, *Yki* activation and subsequent production of inflammatory signals that induce unwarranted ISC proliferation.

Cholinergic receptors regulate ion transport in the mammalian epithelium^{10,25}. We asked whether nAChRs have similar functions in ECs using dyes that detect Na⁺ (SodiumGreen) or Cl[−] (MQAE, 6-methoxyquinolinium derivative, fluorescent indicator for intracellular Cl[−]), and the Ca²⁺ transcriptional reporter NFAT-CalexA²⁶. Reduction of *nAChRβ3* during recovery caused significant ion imbalance in the epithelium, with reduced Cl[−] and Na⁺ levels (Extended Data Fig. 4i). We observed that Ca²⁺ was significantly upregulated the first day of recovery before returning to levels resembling homeostasis (Fig. 3c). This endogenous Ca²⁺ increase disappears when *nAChRβ3* is knocked down in ECs (Fig. 3d). Also, Ca²⁺ increase occurs only in ECs during recovery, as ISCs that use Ca²⁺ for proliferation^{27,28} show Ca²⁺ decline during recovery (Extended Data Fig. 4j). To examine the importance of nAChR-mediated Ca²⁺ during recovery, we genetically compensated for Ca²⁺ in *nAChRβ3*-deficient ECs. Conditional overexpression of Ca²⁺ channel Orai combined with knockdown of *nAChRβ3* in ECs was sufficient to restore (1) ISC proliferation (Fig. 3e and Extended Data Fig. 5a), (2) the number of *pdm1*⁺ ECs (Fig. 3f and Extended Data Fig. 5b) and (3) Cl[−] (Extended Data Fig. 5c) to levels identical to controls. Next, we overexpressed the vertebrate Ca²⁺ buffer protein parvalbumin in ECs to reduce the amount of intracellular Ca²⁺ for 4 days during recovery (Extended Data Fig. 5d). This led to overproliferation during recovery while having no effect during homeostasis (Extended Data Fig. 5d), supporting the importance of Ca²⁺ in ECs during recovery.

To further study the effect of *nAChRβ3* during gut regeneration, we generated flies that overexpress *nAChRβ3* in ECs using the Gal4 or LexA system (*UAS-nAChRβ3* and *LexAopnAChRβ3*; Extended Data Fig. 5e,f). Also, we generated an EC-LexA driver (*mexLexA::GAD*) together with

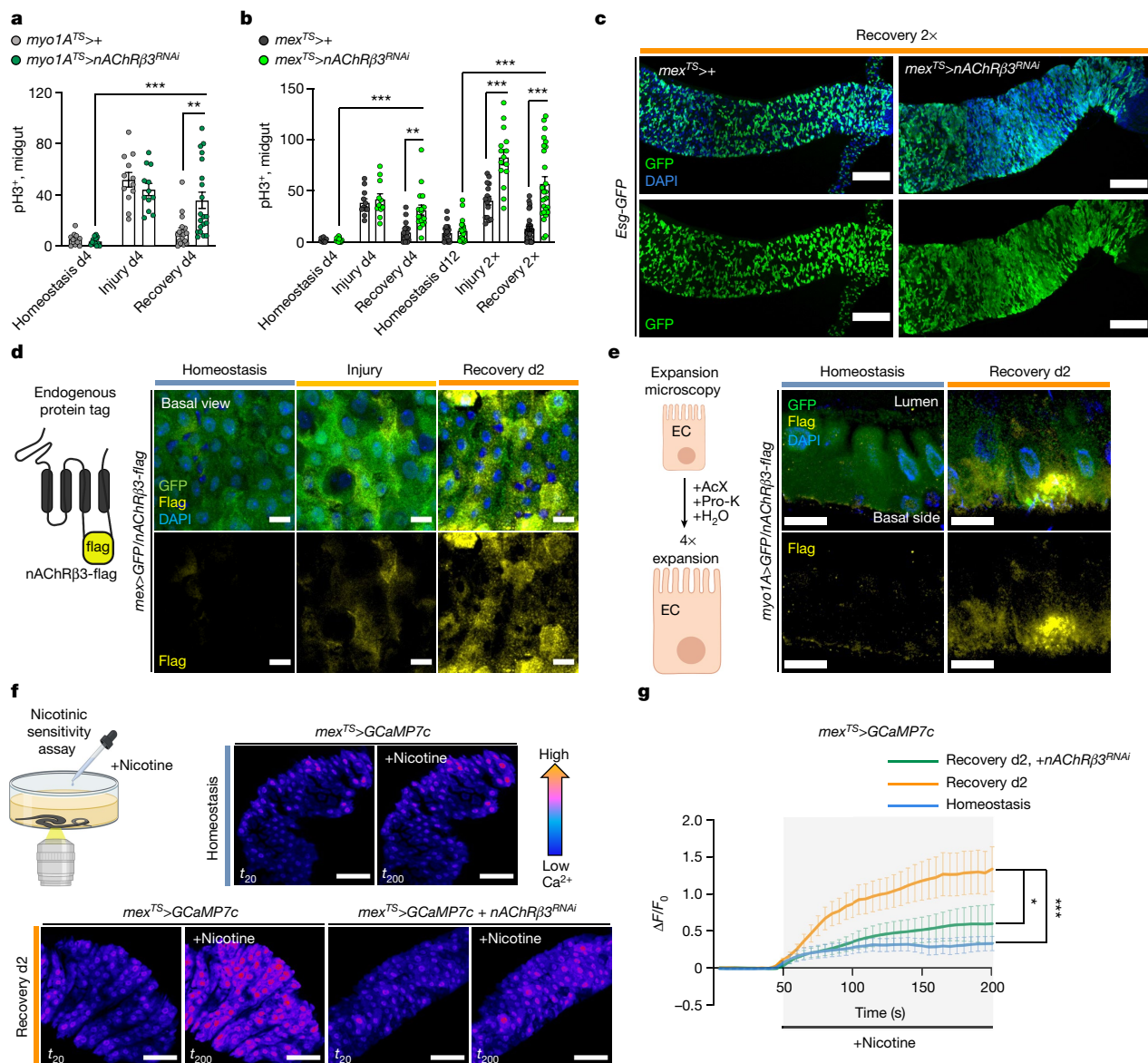


Fig. 2 | nAChRβ3 is required in ECs for recovery. **a**, pH3⁺ counts from midgut of control flies (*myo1A*^{TS/+}) and flies with *nAChRβ3* conditionally reduced in ECs (*myo1A*^{TS/+}*nAChRβ3*^{RNAi}). Control: *n* = 13 (Homeostasis), *n* = 12 (Injury), *n* = 18 (Recovery) guts; *myo1A*^{TS/+}*nAChRβ3*^{RNAi}: *n* = 13 (Homeostasis), *n* = 12 (Injury), *n* = 20 (Recovery) guts, from 2 independent experiments. Sidak's and Tukey's two-way ANOVA, as for Fig. 1e. **b**, pH3⁺ counts from midgut of control flies (*mex*^{TS/+}) and flies with *nAChRβ3* conditionally reduced in ECs (*mex*^{TS/+}*nAChRβ3*^{RNAi}). Control: *n* = 12 (Homeostasis), *n* = 11 (Injury), *n* = 18 (Recovery), *n* = 20 (Homeostasis d12), *n* = 15 (Injury 2x), *n* = 29 (Recovery 2x); *mex*^{TS/+}*nAChRβ3*^{RNAi}: *n* = 12 (Homeostasis), *n* = 11 (Injury), *n* = 17 (Recovery), *n* = 20 (Homeostasis d12), *n* = 15 (Injury 2x), *n* = 26 (Recovery 2x), from 3 independent experiments. Sidak's and Tukey's two-way ANOVA, as for Fig. 1e. **c**, Confocal gut images of *mex*^{TS/+} and *mex*^{TS/+}*nAChRβ3*^{RNAi} flies co-expressing the progenitor cell marker Esg-GFP (green, anti-GFP, as for Fig. 1e). Scale bar, 100 μm. Images are representative of 2 independent experiments with similar results. **d**, Illustration of nAChRβ3-flag and confocal images of midgut expressing nAChRβ3-flag and GFP-expressing

ECs (*mex*>*GFP*). anti-Flag: nAChRβ3-flag (yellow); anti-GFP: ECs (green). Scale bar, 10 μm. Images are representative of 3 independent experiments with similar results, as for Fig. 1e. **e**, Illustration followed by images of expanded midguts from flies expressing nAChRβ3-flag (yellow) and GFP-expressing ECs (*myo1A*>*GFP*, green). Scale bar, 50 μm. Images are representative of 2 independent experiments with similar results. **f**, Illustration and colour-coded sequential frames of midgut before (*t*₂₀) and after (*t*₂₀₀) nicotine administration of *mex*^{TS/+}*GCaMP7c* and *mex*^{TS/+}*GCaMP7c* + *nAChRβ3*^{RNAi} flies (Supplementary Videos 4–6). **g**, Average relative fluorescence intensity ($\Delta F/F_0$) per frame (5 s per frame) per condition and genotype of midguts, as described in **f**. *n* = 7 (Homeostasis), *n* = 7 (Recovery d2), *n* = 5 (Recovery d2, *mex*^{TS/+}*Ace*) guts from 2 independent experiments. Tukey's two-way ANOVA (Recovery d2 versus Recovery d2 + *nAChRβ3*^{RNAi}, *P* = 0.0116), as for Fig. 1g. Scale bar, 50 μm. Individual $\Delta F/F_0$ values are shown in Extended Data Fig. 3k. DAPI: nuclei. *0.05 > *P* > 0.01, **0.01 < *P* < 0.001, ****P* < 0.001. Mean ± s.e.m. Illustrations in **d**, **e** and **f** created using BioRender.com.

Tubulin-Gal80^{TS}, referred to as *mexLexA*^{TS} (Extended Data Fig. 5f). Conditionally overexpressing *nAChRβ3* in ECs during homeostasis doubles the amount of Ca²⁺ in ECs after nicotine administration (Extended Data Fig. 5g). Also, *nAChRβ3* overexpression in ECs significantly expedited recovery, with ISC proliferation and *pdm1* expression reaching levels indistinguishable from unchallenged guts at 2 days, half the expected time (Fig. 3g,h). *nAChRβ3* overexpression in ECs during homeostasis

and injury did not change ISC proliferation (Fig. 3g). Additionally, overexpressing *nAChRβ3* in ECs during recovery significantly reduced inflammatory cytokine levels and cell death (Fig. 3i and Extended Data Fig. 5h–j).

Together, our data show that high intracellular Ca²⁺ levels in ECs triggered by nAChRs control intestinal epithelium recovery by promoting EC maturation and ion balance. Disruption of nAChR-mediated

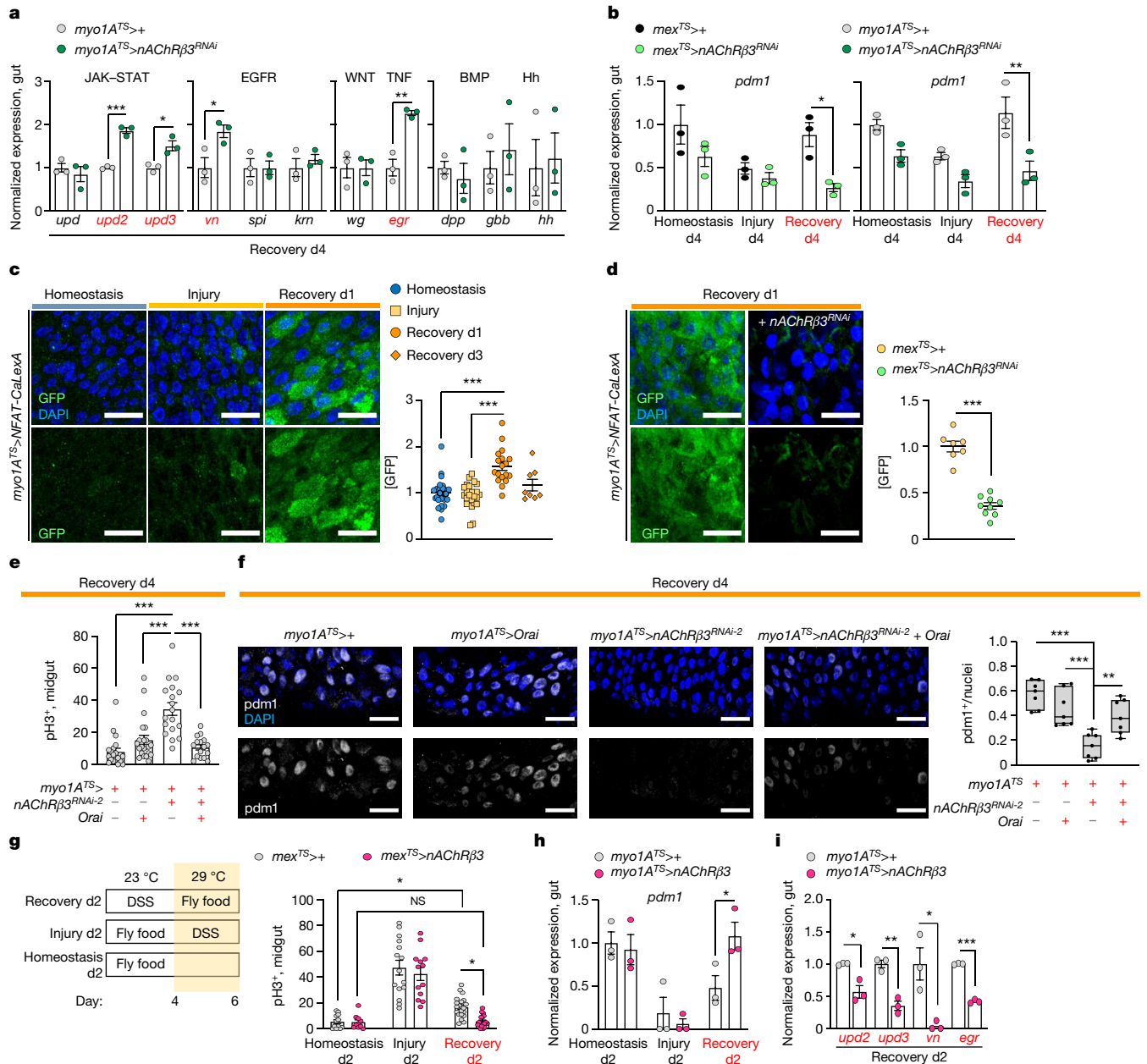


Fig. 3 | nAChRβ3-mediated Ca^{2+} promotes recovery. **a**, Cytokine expression levels when reducing *nAChRβ3* in ECs (*myo1A^{TS}>nAChRβ3^{RNAi}*), similar to Fig. 1e. *upd*, *unpaired*; *vn*, *vein*; *spl*, *spitz*; *krm*, *keren*; *wg*, *wingless*; *dpp*, *decapentaplegic*; *gbb*, *glass bottom boat*; *hh*, *hedgehog*. *n* = 3 biologically independent samples per genotype. Sidak's two-way ANOVA; *P* = 0.0196 (*vn*), *P* = 0.0022 (*egr*). **b**, *pdm1* levels when reducing *nAChRβ3* in ECs (*mex^{TS}>nAChRβ3^{RNAi}* and *myo1A^{TS}>nAChRβ3^{RNAi}*). Similar to Fig. 1e. *n* = 3 biologically independent samples per genotype and condition. Sidak's two-way ANOVA; *P* = 0.0014 (Recovery d4, *myo1A^{TS}>* versus *myo1A^{TS}>nAChRβ3^{RNAi}*), *P* = 0.0142 (Recovery d4, *mex^{TS}>* versus *mex^{TS}>nAChRβ3^{RNAi}*). **c**, Posterior midgut with *Ca²⁺* reporter in ECs (*myo1A^{TS}>NFAT-CaLexA*). Reporter expression: 2 days (29 °C) per condition. GFP: green (*Ca²⁺*). Graph: GFP per image and condition. *n* = 25 (Homeostasis), *n* = 24 (Injury), *n* = 18 (Recovery d1), *n* = 8 (Recovery d3) guts, from 3 independent experiments (Dunn's Kruskal–Wallis test). **d**, Posterior midgut with NFAT-CaLexA in control (*mex^{TS}>NFAT-CaLexA*) and when reducing *nAChRβ3* in ECs (*mex^{TS}>nAChRβ3^{RNAi}*). Conditions: 4 days DSS food (23 °C) and standard food for 24 h (29 °C). *n* = 7 (control), *n* = 9 (*nAChRβ3^{RNAi}*) guts, from 2 independent experiments (two-tailed *t*-test). **e**, pH3⁺ counts from *Orai* (*Ca²⁺* channel) overexpression (*myo1A^{TS}>Orai*), *nAChRβ3* reduction (*myo1A^{TS}>nAChRβ3^{RNAi-2}*)

and combined (*myo1A^{TS}>nAChRβ3^{RNAi} + Orai*) in ECs. Similar to Fig. 1e. *n* = 20 (control), *n* = 22 (*Orai*), *n* = 18 (*nAChRβ3^{RNAi-2}*), *n* = 16 (*nAChRβ3^{RNAi} + Orai*) guts, from 3 independent experiments (Dunn's Kruskal–Wallis test). **f**, Posterior midgut stained with anti-*pdm1* (grey), as for **e**. Boxplot: *pdm1*⁺ versus all nuclei per image (median, quartiles, whiskers: minimum and maximum values). *n* = 7 guts per genotype (Tukey's one-way ANOVA, *Orai* versus *nAChRβ3^{RNAi} + Orai*: *P* = 0.0092), from 2 independent experiments. **g**, Experimental design and pH3⁺ counts when *nAChRβ3* is overexpressed in ECs (*mex^{TS}>nAChRβ3*). Control: *n* = 12 (Homeostasis), *n* = 15 (Injury), *n* = 21 (Recovery d2) guts; *mex^{TS}>nAChRβ3*: *n* = 8 (Homeostasis), *n* = 13 (Injury), *n* = 18 (Recovery d2) guts, from 2 independent experiments. Two-way ANOVA: *P* = 0.023 (Recovery d2: control versus *mex^{TS}>nAChRβ3*), *P* = 0.0396 (control: Homeostasis versus Recovery d2). **h**, *pdm1* levels from *myo1A^{TS}>nAChRβ3* flies similar to **g**. *n* = 3 biologically independent samples per genotype. Sidak's two-way ANOVA (*pdm1*/Recovery d2: *P* = 0.0415). **i**, Cytokine levels from guts of flies, as in **h**. *n* = 3 biological independent samples per genotype. Sidak's two-way ANOVA (*upd2*: *P* = 0.0326, *upd3*: *P* = 0.0014, *egr*: *P* = 0.0037). DAPI: nuclei. Scale bars, 20 μm. *0.05 > *P* > 0.01, **0.01 < *P* < 0.001, ****P* < 0.001. Mean ± s.e.m.

Ca²⁺ causes EC deficiency, ion imbalance, elevated cell death and Yki activation, followed by overinflammation and overproliferation. By contrast, increasing Ca²⁺ in ECs by means of overexpressing *nAChRβ3* expedites return to homeostasis by advancing EC maturation and decreasing cell death, subsequently reducing inflammation and proliferation.

Neuro–EC interactions promote recovery

ACh is released by neuronal and non-neuronal cells that express *ChAT* (*Choline acetyltransferase*), the enzyme that catalyses ACh synthesis³. To identify the source of ACh responsible for nAChR-mediated recovery, we first tested midgut cells (progenitor cells, ECs, enteroendocrine cells), the visceral muscle and immune cells (haemocytes). ISC proliferation during recovery remained unaffected when *ChAT* was conditionally knocked down in these cells (Extended Data Fig. 6a). Similarly, enteroendocrine-cell-less guts²⁹ do not overproliferate during recovery (Extended Data Fig. 6b). Altogether, these data point to a neuronal source of ACh. The importance of neurons during regeneration has been reported in different tissues³⁰. For the gut, studies have highlighted the anti-inflammatory properties of mammalian enteric neurons^{31,32}, whereas limited associations have been made between neurons and ISC proliferation in *Drosophila*^{33,34}.

Because ACh is a short-distance neurotransmitter/local neurohormone, the most likely source during recovery is the enteric nervous system. *Drosophila* enteric neurons innervate the midgut in anterior (R1, R2) and posterior regions (R4, R5), even though their cell bodies reside in the brain, hypocerebral ganglion or adult ventral nerve cord (VNC)². Also, enteric innervations reach the intestinal epithelium³⁴. To identify a driver for cholinergic enteric neurons, we screened a set of neuronal drivers (FlyLight)³⁵. We identified a Gal4 driver, *R49E06-Gal4*, which is expressed in about 43 neurons in the abdominal ganglion of the VNC (Extended Data Fig. 6c–g), has no expression in the gut and has very limited expression in the brain (Extended Data Fig. 6c & FlyLight). We tested the cholinergic nature of *R49E06* neurons using the cholinergic Gal80 repressor (ChAT-Gal80), which inhibited GFP expression in most VNC *R49E06* neurons (Extended Data Fig. 6d). We found that around 35 of the approximately 43 neurons in the abdominal ganglia are cholinergic (expressing ChAT) (Extended Data Fig. 6e,f), and most do not express Prospero (Pros; Extended Data Fig. 6g). We observed that some *R49E06* neurons innervate the midgut and are ChAT⁺ (Extended Data Fig. 6h), indicating that a subpopulation of *R49E06* neurons are cholinergic enteric neurons. To confirm that *R49E06* innervations can release ACh to the gut, we used an antibody against the synaptic vesicle membrane protein Synaptotagmin 1 (Syt1), which is essential for neurotransmitter release. We observed that *R49E06* innervations run between the muscle and intestinal epithelium while carrying Syt1⁺ swellings (Extended Data Fig. 6i). We refer to Syt1⁺ swellings as presynaptic boutons because they resemble en passant varicosities described in the autonomous nervous system and are located at sites where a neurotransmitter diffuses to receptors located in nearby (innervated) cells. Together, these data indicate that *R49E06* neurons are in their majority cholinergic and include a subpopulation of cholinergic enteric neurons that innervate the intestinal epithelium and muscle.

To further characterize *R49E06* enteric innervations, we sectioned flies with a vibratome so that innervations and gut remained intact (Fig. 4a). *R49E06* neurons innervate the midgut at distinct locations in R2, R4 and R5 (Fig. 4a). To distinguish between the axonal and dendritic domains, we expressed the synaptic vesicle marker Syt1HA and the dendritic indicator DenMark for 2 days during recovery. We observed that Syt1HA accumulated at the terminal of *R49E06* innervations in the vicinity of the gut (Fig. 4a and Extended Data Fig. 6j), whereas DenMark accumulated upstream (Extended Data Fig. 6k). We observed that Syt1HA innervations are close to ECs (Fig. 4b, Extended Data Fig. 6l and

Supplementary Video 7), indicating that *R49E06* neurons innervate ECs and could be the source of ACh.

To test whether *R49E06* neurons regulate gut regeneration, we conditionally knocked down *ChAT* in these neurons. This caused: (1) overproliferation during recovery and after repetitive DSS injury (Fig. 4c); (2) recovery-specific reduction of *pdm1* (Fig. 4d); (3) no significant change of *pros* (Extended Data Fig. 7a); and (4) elevated expression of inflammatory cytokines during recovery (Extended Data Fig. 7b). Also, co-expression of the VNC repressor *Tsh-Gal80* (ref. 36), while reducing *ChAT* in *R49E06* neurons, prevented ISC overproliferation during recovery (Extended Data Fig. 7c). Further, *ChAT* decrease in *R49E06* neurons led to ISC overproliferation after *Ecc15* infection (Extended Data Fig. 7d). Thus, reduction of ACh synthesis from *R49E06* neurons in VNC leads to lasting unresolved injury, resembling *nAChRβ3* deficiency in ECs. These data indicate that intestinal repair is under neuronal control, leading us to name these neurons ARCENs.

To test whether ARCENs are required for nAChR-mediated recovery, we blocked neurotransmitter release with the *UAS-shibire^{TS}* transgene while simultaneously overexpressing *nAChRβ3* (Fig. 4e). We found that 24 h of expression of *shibire^{TS}* in ARCENs was sufficient to prevent *nAChRβ3* overexpression in ECs from rapidly decreasing proliferation (Fig. 4e). To verify that ARCENs release ACh to the intestinal epithelium, we overexpressed the ion channel TrpA1 and thermo-genetically depolarized ARCENs (Extended Data Fig. 7e). TrpA1-mediated induction of ARCENs in the first 6 h of recovery significantly reduced ISC proliferation, whereas additionally expressing the cholinergic repressor *ChAT-Gal80* restored proliferation to levels identical to controls (Extended Data Fig. 7e). Also, TrpA1-induction of ARCENs significantly reduced the expression of gut inflammatory cytokines (Extended Data Fig. 7f). Moreover, we used the binary expression Q-system to generate the *R49E06-QF* (ARCEN-QF) driver (Extended Data Fig. 7g). We used ARCEN-QF together with light-gated cation channel CsChrimson to depolarize ARCENs while conditionally expressing in ECs the Ca²⁺ transcriptional reporter *NFAT-CaLexA* (Fig. 4f). Optogenetic activation of ARCENs in the first 6 h of recovery was sufficient to significantly increase endogenous Ca²⁺ and levels of *pdm1⁺* ECs (Fig. 4f). Together, these data support that ARCENs provide ACh to ECs to promote transition to homeostasis after injury by activating nAChR-mediated Ca²⁺ influx, increasing mature ECs, reducing proliferation and decreasing inflammation in the intestinal epithelium. However, we cannot completely rule out that the subpopulation of ARCENs without enteric innervations may have mediator roles that promote recovery by activating non-ARCEN cholinergic enteric innervations. Our findings demonstrate nerve-dependent intestinal regeneration, placing the intestinal epithelium among the tissues whose ability to regenerate depends on neurons.

ARCENs depend on TNF signalling

The cholinergic anti-inflammatory reflex has been proposed to sense inflammatory signals such as TNF and reduce them by triggering ACh release across neuro–immune interactions^{11,37}. As *Drosophila* peripheral neurons have been reported to respond to Egr through *wengen* (*wgn*)³⁸, one of the two known Egr receptors (*wgn* and *grindelwald*, *grnd*)^{39,40}, we tested whether the protective role of ARCENs is linked to Egr. Reduction of *wgn* but not *grnd* in ARCENs led to significant ISC overproliferation specifically during recovery, which was rescued when *Tsh-Gal80* was co-expressed (Fig. 4g and Extended Data Fig. 7h).

We searched for the source of TNF signalling by conditionally knocking down *egr* in gut and immune cells (Extended Data Fig. 7i). Reduction of *egr* in progenitor cells and ECs did not impact ISC proliferation during recovery and knocking down *egr* in haemocytes caused under-proliferation (Extended Data Fig. 7i). However, decreasing *egr* in all three populations concurrently caused significant overproliferation during recovery (Extended Data Fig. 7i,j). This indicates that ARCENs

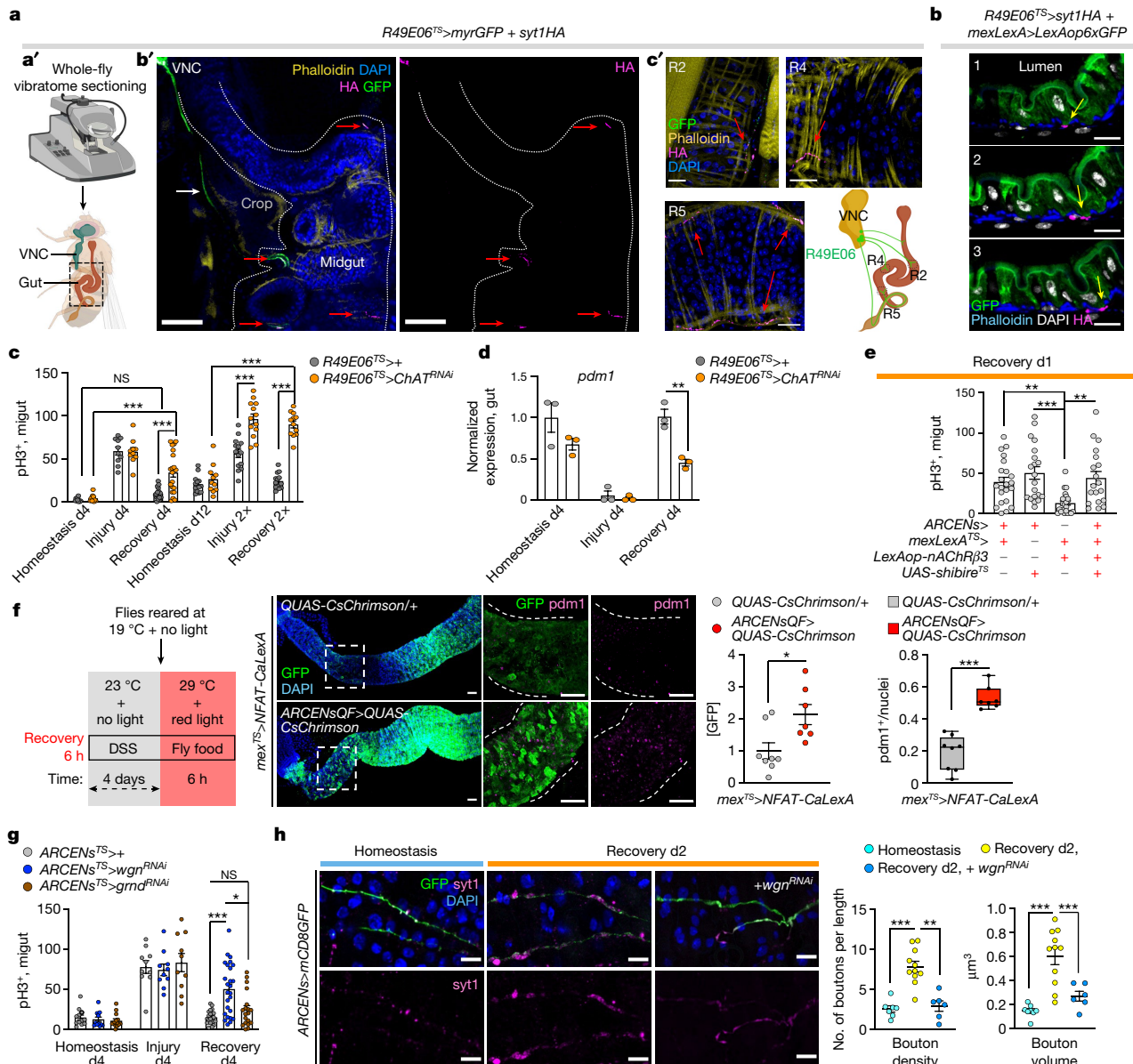


Fig. 4 | ARCEN-EC interactions promote recovery. **a**, Vibratome sectioning of *R49E06^{TS}>myrGFP + syt1HA* flies (Recovery d2). **a'**, **b'**, Sectioned thorax/abdomen (square). White dots, midgut; white arrow, R49E06-projection. **c'**, Innervated R2, R4, R5. anti-GFP: R49E06 innervations (green); anti-HA: R49E06 innervations expressing the presynaptic marker syt1HA (magenta). Red arrow, R49E06 enteric innervations. Images **b'** and **c'** are representative of 2 independent experiments with similar results. Scale bars, 100 μ m (**b'**), 20 μ m (**c'**). **b**, Sequential R4 images (Supplementary Video 7) from *R49E06^{TS}>syt1HA + mexLexA>6xLexAopGFP* flies (Recovery d2). Arrows, anti-HA: R49E06 innervation expressing the presynaptic marker syt1HA (magenta); anti-GFP: ECs (green). Scale bar, 10 μ m. Images are representative of 2 independent experiments with similar results. **c**, pH3⁺ counts when *ChAT* is reduced in *R49E06* neurons (*R49E06^{TS}>ChAT^{RNAi}*). Control: *n* = 10 (Homeostasis), *n* = 10 (Injury), *n* = 16 (Recovery d4), *n* = 13 (Homeostasis d12), *n* = 14 (Injury 2 \times), *n* = 13 (Recovery 2 \times) guts; *R49E06^{TS}>ChAT^{RNAi}*: *n* = 10 (Homeostasis), *n* = 10 (Injury), *n* = 20 (Recovery d4), *n* = 11 (Homeostasis d12), *n* = 13 (Injury 2 \times), *n* = 12 (Recovery 2 \times) guts, from 2 independent experiments (Sidak's two-way ANOVA). Similar to Fig. 1e, f. **d**, *pdm1* expression levels. *n* = 3 biologically independent samples. Sidak's two-way ANOVA (*P* = 0.0027). **e**, pH3⁺ counts when overexpressing *nAcr β* in ECs (*mexLexA^{TS}>lexAop-nAcr β*) and thermo-silencing (>27 $^{\circ}$ C) *R49E06* neurons (referred to as ARCENs) with *shibire^{TS}* (*ARCENs>shibire^{TS}*). Conditions: 4 days of DSS food (23 $^{\circ}$ C), 24 h of standard food (29 $^{\circ}$ C). *n* = 22 (control), *n* = 20

(*ARCENs>shibire^{TS}*), *n* = 24 (*mexLexA^{TS}>lexAop-nAcr β*), *n* = 19 (*ARCENs>shibire^{TS} + mexLexA^{TS}>lexAop-nAcr β*) guts, from 3 independent experiments. Dunn's Kruskal-Wallis test: *P* = 0.0029 (control versus *shibire^{TS}*), *P* = 0.0024 (*shibire^{TS} + lexAop-nAcr β* versus *shibire^{TS}*). **f**, Thermo- and optogenetic induction with NFAT-CalexA expressed in ECs (*mex^{TS}>NFAT-CalexA/QUAS-CsChrimson*) after depolarizing ARCENs with CsChrimson (*mex^{TS}>NFAT-CalexA/ARCENsQF>QUAS-CsChrimson*). anti-GFP, Ca²⁺ (green); anti-pdm1, ECs (magenta). Chart: GFP fold-change; boxplot: pdm1⁺ ratio (median, quartiles, whiskers: minimum and maximum values). *n* = 8 (control), *n* = 7 (CsChrimson) guts, from 2 independent experiments; two-tailed Mann-Whitney test (*P* = 0.0205/GFP). Scale bar, 50 μ m. **g**, pH3⁺ counts after reducing TNF receptors in ARCENs (*wgn*, *ARCENs^{TS}>wgn^{RNAi}*; *grnd*, *ARCENs^{TS}>grnd^{RNAi}*). Control: *n* = 12 (Homeostasis), *n* = 10 (Injury), *n* = 21 (Recovery); *wgn^{RNAi}*: *n* = 12 (Homeostasis), *n* = 10 (Injury), *n* = 25 (Recovery); *grnd^{RNAi}*: *n* = 14 (Homeostasis), *n* = 10 (Injury), *n* = 19 (Recovery) guts, from 2 independent experiments. Dunn's Kruskal-Wallis test: *P* = 0.0185 (*wgn^{RNAi}* versus *grnd^{RNAi}*; Recovery). **h**, R5 of *ARCENs>mCD8GFP* and *ARCENs>mCD8GFP + wgn^{RNAi}* guts. anti-GFP, ARCENs innervations (green); anti-Syt1, boutons (magenta). *n* = 8 (Homeostasis), *n* = 11 (Recovery), *n* = 6 (*wgn^{RNAi}*) guts, from 2 independent experiments. Tukey's one-way ANOVA (*P* = 0.0019, Recovery versus *wgn^{RNAi}*; boutons). Scale bar, 10 μ m. Phalloidin: muscle; DAPI: nuclei. *0.05 > *P* > 0.01, **0.01 < *P* < 0.001, ****P* < 0.001. Mean \pm s.e.m. Illustrations in a created using BioRender.com.

probably sense Egr from several sources. Also, knocking down *egr* in all three cell populations during injury caused ISC under-proliferation (Extended Data Fig. 7j), consistent with the proposed proliferative role of Egr⁴¹.

Further, we tested whether secreted Egr reaches ARCENs. We expressed in the transmembrane of ARCENs an extracellular nanobody-based GFP trap (morphotrap)⁴² for 2 days during recovery while endogenous Egr was fused to GFP (Egr–GFP). We observed GFP accumulation in ARCEN projections expressing the morphotrap (Extended Data Fig. 7k), indicating that secreted Egr reaches ARCENs. GFP accumulation was observed only in ARCEN projections near the posterior midgut and not near the VNC (Extended Data Fig. 7k). Because near the posterior midgut ARCEN innervations are enriched with dendritic sites (Extended Data Fig. 6k), this raises the possibility that wgn receptors are present in this region, and ARCENs probably sense Egr through their enteric projections during recovery. As TNF has been proposed to promote synaptic plasticity and strengthening⁴³ and axonal strengthening is associated with elevated firing⁴⁴, we examined whether existing synaptic boutons of ARCEN innervations undergo Egr-dependent changes (Fig. 4h). ARCEN innervations undergo significant increase in density and volume of synaptic boutons during recovery compared with homeostasis (Fig. 4h). This increase is diminished upon *wgn* reduction (Fig. 4h), indicating that ARCEN innervations respond to Egr by strengthening their axonal properties, probably to boost ACh release. Altogether, our data support that the function of ARCENs during gut regeneration is linked to TNF signalling, reminiscent of the cholinergic anti-inflammatory reflex³⁷.

Ca²⁺ spreads via *Inx2*–*Inx7* gap junctions

We observed that opto-activation of ARCENs led to broad Ca²⁺ increase across ECs in the posterior gut (Fig. 4f), despite the limited innervations, indicating that Ca²⁺ probably propagates between innervated and non-innervated ECs. To test this, we performed *ex vivo* Ca²⁺ live imaging utilizing split-Gal4 drivers⁴⁵ that when combined are specific to a small population of ECs between R4 and R5 (R4c; Extended Data Fig. 8a), which we refer as spECs. We transiently increased Ca²⁺ in spECs using the light-gated CsChrimson channel, while recording Ca²⁺ changes in neighbouring ECs (Fig. 5a and Extended Data Fig. 8b). Activation of CsChrimson in spECs increased Ca²⁺ in distant ECs as far as 180 μ m (Fig. 5a, Extended Data Fig. 8b and Supplementary Video 8), and the gap junction blocker Heptanol significantly reduced Ca²⁺ propagation (Extended Data Fig. 8b). These data indicate that when Ca²⁺ is elevated in a subpopulation of ECs, gap junctions spread Ca²⁺ in more ECs. The endogenous flow of ions among cells (bioelectric signalling) has been proposed to regulate regeneration^{9,46,47}. Therefore, we tested whether generating Ca²⁺ currents by means of CsChrimson activation in spECs could affect gut regeneration (Fig. 5b). We found that 7 h of opto-activation of spECs led to a significantly faster decrease in proliferation on the first day of recovery (Fig. 5b), reminiscent of ARCEN activation (Extended Data Fig. 7e).

To investigate further how bioelectric signalling regulates gut recovery, we analysed in our single-nuclei data the expression of innexins, the components of gap junctions in invertebrates^{6,48}. *Inx2* and *Inx7* are similarly enriched in ECs whereas their expression in progenitor cell and enteroendocrine cell clusters is lower (Extended Data Fig. 8c–e). We confirmed expression in ECs using an antibody for *Inx2* (Extended Data Fig. 8f). *Inx7* reduction in ECs disrupted *Inx2* gap junction formation (Extended Data Fig. 8g,h), indicating that *Inx2* and *Inx7* form heteromeric gap junctions. Moreover, knocking down *Inx2* or *Inx7* in ECs led to recovery-specific overproliferation (Fig. 5c,d), whereas no significant changes occurred during homeostasis or injury. Further, knocking down *Inx2* while opto-activating spECs prevented rapid decrease in ISC

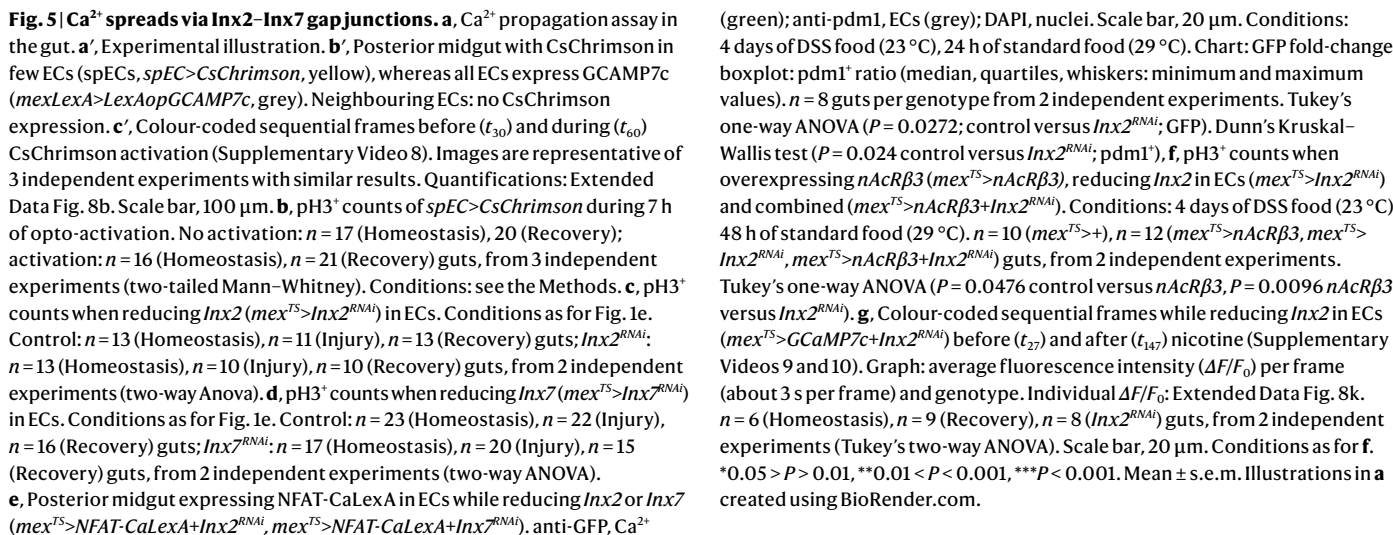
proliferation during recovery (Extended Data Fig. 8i). Also, knocking down *Inx2* or *Inx7* in ECs during recovery caused significantly reduced and irregular Ca²⁺ distribution together with significantly decreased pdm1⁺ levels (Fig. 5e).

Gap junctions are activated by membrane potential changes, including increases in intracellular Ca²⁺ (ref. 6). This indicates that nAChR-induced Ca²⁺ during recovery could prompt gap junction activation in ECs. To test this, we overexpressed *nAChR β 3* for 2 days while knocking down *Inx2* in ECs during recovery (Fig. 5f and Extended Data Fig. 8j). Knocking down *Inx2* was sufficient to attenuate rapid decrease in ISC proliferation and block fast increase of pdm1⁺ ECs, thereby blocking the expedited recovery triggered by *nAChR β 3* overexpression (Fig. 5f and Extended Data Fig. 8j). Finally, we tested whether *Inx2*–*Inx7* gap junctions facilitated Ca²⁺ responses in ECs during the nicotinic sensitivity assay. Conditionally reducing *Inx2* expression resulted in significantly dampened nicotine-triggered Ca²⁺ increase during recovery (Fig. 5g, Extended Data Fig. 8k and Supplementary Videos 9 and 10). We observed that Ca²⁺ distribution among ECs was not only reduced but also uneven (Fig. 5g, Extended Data Fig. 8k and Supplementary Videos 9 and 10). This indicates that during recovery gap junctions facilitate nAChR-induced Ca²⁺ to spread evenly among ECs. Altogether, our data support that *Inx2*–*Inx7* gap junctions are required for nAChR-mediated Ca²⁺ to spread in ECs during recovery and that disruption of this bioelectric signalling prevents transition to homeostasis.

Discussion

We address a fundamental question, how does transition to homeostasis occur after injury? We found that the cholinergic pathway directs the gut to return to homeostasis by coordinating neuro–epithelial interactions and bioelectric signalling (Extended Data Fig. 9). Our findings reveal that nAChR-mediated high Ca²⁺ in ECs is essential for recovery (Fig. 3 and Extended Data Fig. 5). It is reported that Ca²⁺ increase after nAChR activation is augmented autonomously by opening of voltage-gated Ca²⁺ channels and release of Ca²⁺ from intracellular stores⁴⁹. This could occur in nAChR-activated ECs during recovery, probably to assist in sufficiently elevating Ca²⁺. We discovered that elevated Ca²⁺ from few ECs spreads via gap junctions to more ECs (Fig. 5 and Extended Data Fig. 8), which is consistent with a recent report of Ca²⁺ waves in R3 of the midgut⁵⁰. The use of endogenous ion currents that electrically couple several cells so that they behave as one unit has been linked to growth and tissue-patterning during development and regeneration^{9,47}. Our study supports that bioelectric mechanisms regulate midgut regeneration to ensure that important physiological functions such as ion transport are evenly restored across the epithelium.

Despite the increasing knowledge of protective anti-inflammatory roles for peripheral neurons, many aspects remain unclear¹¹. We discovered that cholinergic signalling from ARCENs is required for the transition of the intestinal epithelium from injury to homeostasis (Fig. 4 and Extended Data Fig. 7). During recovery ARCEN innervations undergo Egr-dependent synaptic strengthening (Fig. 4h) and ECs change the levels of cholinergic components (Figs. 1d and 2d,e). This coordinated plasticity in neuro–epithelial cholinergic interactions probably occurs to control the initiation, strength and duration of nAChR-mediated Ca²⁺ currents across the epithelium and to precisely promote recovery. In addition, the cholinergic anti-inflammatory reflex has been proposed to be a cholinergic neuro–immune response that senses and counteracts inflammatory signals^{11,37}. We propose that a similar mechanism exists in *Drosophila* and is regulated by ARCENs that reside in the posterior VNC, potentially the fly equivalent of the vagus nerve. ARCENs sense Egr probably through their projections (Extended Data Figs. 6k and 7k) and counteract gut inflammation and proliferation by means of neuro–EC cholinergic signalling (Fig. 4 and



directs a tissue towards homeostasis. This work may help identify the aetiology of chronic intestinal diseases and provides a link between neurological disorders and intestinal pathologies.

Online content

Any methods, additional references, Nature Portfolio reporting summaries, source data, extended data, supplementary information, acknowledgements, peer review information; details of author contributions and competing interests; and statements of data and code availability are available at <https://doi.org/10.1038/s41586-023-06627-y>.

- Karin, M. & Clevers, H. Reparative inflammation takes charge of tissue regeneration. *Nature* **529**, 307–315 (2016).
- Miguel-Aliaga, I., Jasper, H. & Lemaitre, B. Anatomy and physiology of the digestive tract of *Drosophila melanogaster*. *Genetics* **210**, 357–396 (2018).
- Wessler, I. & Kirkpatrick, C. J. Acetylcholine beyond neurons: the non-neuronal cholinergic system in humans. *Br. J. Pharmacol.* **154**, 1558–1571 (2008).
- Wiesner, J., Kriz, Z., Kuca, K., Jun, D. & Koca, J. Acetylcholinesterases—the structural similarities and differences. *J. Enzyme Inhib. Med. Chem.* **22**, 417–424 (2007).
- Igaki, T. et al. Eiger, a TNF superfamily ligand that triggers the *Drosophila* JNK pathway. *EMBO J.* **21**, 3009–3018 (2002).
- Guiza, J., Barria, I., Saez, J. C. & Vega, J. L. Innexins: expression, regulation, and functions. *Front. Physiol.* **9**, 1414 (2018).
- Snigdha, K., Gangwani, K. S., Lapalikar, G. V., Singh, A. & Kango-Singh, M. Hippo signaling in cancer: lessons from *Drosophila* models. *Front. Cell Dev. Biol.* **7**, 85 (2019).
- Subramanian, S., Geng, H. & Tan, X. D. Cell death of intestinal epithelial cells in intestinal diseases. *Sheng Li Xue Bao* **72**, 308–324 (2020).
- Levin, M. Bioelectric signaling: reprogrammable circuits underlying embryogenesis, regeneration, and cancer. *Cell* **184**, 1971–1989 (2021).
- Hirota, C. L. & McKay, D. M. Cholinergic regulation of epithelial ion transport in the mammalian intestine. *Br. J. Pharmacol.* **149**, 463–479 (2006).
- Goverse, G., Stakenborg, M. & Matteoli, G. The intestinal cholinergic anti-inflammatory pathway. *J. Physiol.* **594**, 5771–5780 (2016).
- Panayidou, S. & Apidianakis, Y. Regenerative inflammation: lessons from *Drosophila* intestinal epithelium in health and disease. *Pathogens* **2**, 209–231 (2013).
- Micchelli, C. A. & Perrimon, N. Evidence that stem cells reside in the adult *Drosophila* midgut epithelium. *Nature* **439**, 475–479 (2006).
- Ohlstein, B. & Spradling, A. The adult *Drosophila* posterior midgut is maintained by multipotent stem cells. *Nature* **439**, 470–474 (2006).
- Jiang, H., Tian, A. & Jiang, J. Intestinal stem cell response to injury: lessons from *Drosophila*. *Cell. Mol. Life Sci.* **73**, 3337–3349 (2016).
- Guo, Z., Driver, I. & Ohlstein, B. Injury-induced BMP signaling negatively regulates *Drosophila* midgut homeostasis. *J. Cell Biol.* **201**, 945–961 (2013).
- Tracy Cai, X. et al. AWD regulates timed activation of BMP signaling in intestinal stem cells to maintain tissue homeostasis. *Nat. Commun.* **10**, 2988 (2019).
- Agaisse, H., Petersen, U. M., Boutros, M., Mathey-Prevot, B. & Perrimon, N. Signaling role of hemocytes in *Drosophila* JAK/STAT-dependent response to septic injury. *Dev. Cell* **5**, 441–450 (2003).
- Buchon, N. et al. Morphological and molecular characterization of adult midgut compartmentalization in *Drosophila*. *Cell Rep.* **3**, 1725–1738 (2013).
- Tian, A., Wang, B. & Jiang, J. Injury-stimulated and self-restrained BMP signaling dynamically regulates stem cell pool size during *Drosophila* midgut regeneration. *Proc. Natl Acad. Sci. USA* **114**, E2699–E2708 (2017).
- Dana, H. et al. High-performance calcium sensors for imaging activity in neuronal populations and microcompartments. *Nat. Methods* **16**, 649–657 (2019).
- Li, M., Sun, S., Priest, J., Bi, X. & Fan, Y. Characterization of TNF-induced cell death in *Drosophila* reveals caspase- and JNK-dependent necrosis and its role in tumor suppression. *Cell Death Dis.* **10**, 613 (2019).
- Karpowicz, P., Perez, J. & Perrimon, N. The Hippo tumor suppressor pathway regulates intestinal stem cell regeneration. *Development* **137**, 4135–4145 (2010).
- Ren, F. et al. Hippo signaling regulates *Drosophila* intestine stem cell proliferation through multiple pathways. *Proc. Natl Acad. Sci. USA* **107**, 21064–21069 (2010).
- Dolan, B., Ermund, A., Martinez-Abad, B., Johansson, M. E. V. & Hansson, G. C. Clearance of small intestinal crypts involves goblet cell mucus secretion by intracellular granule rupture and enterocyte ion transport. *Sci. Signal.* **15**, eabl5848 (2022).
- Masuyama, K., Zhang, Y., Rao, Y. & Wang, J. W. Mapping neural circuits with activity-dependent nuclear import of a transcription factor. *J. Neurogenet.* **26**, 89–102 (2012).
- Deng, H., Gerencser, A. A. & Jasper, H. Signal integration by Ca^{2+} regulates intestinal stem-cell activity. *Nature* **528**, 212–217 (2015).
- Xu, C., Luo, J., He, L., Montell, C. & Perrimon, N. Oxidative stress induces stem cell proliferation via TRPA1/RyR-mediated Ca^{2+} signaling in the *Drosophila* midgut. *eLife* <https://doi.org/10.7554/eLife.22441> (2017).
- Amcheslavsky, A. et al. Enterendocrine cells support intestinal stem-cell-mediated homeostasis in *Drosophila*. *Cell Rep.* **9**, 32–39 (2014).
- Kumar, A. & Brookes, J. P. Nerve dependence in tissue, organ, and appendage regeneration. *Trends Neurosci.* **35**, 691–699 (2012).
- Lai, N. Y. et al. Gut-innervating nociceptor neurons regulate Peyer's patch microfold cells and SFB levels to mediate *Salmonella* host defense. *Cell* **180**, 33–49 e22 (2020).
- Matheis, F. et al. Adrenergic signaling in *muscularis* macrophages limits infection-induced neuronal loss. *Cell* **180**, 64–78 e16 (2020).
- Han, H. et al. Gut-neuron interaction via Hh signaling regulates intestinal progenitor cell differentiation in *Drosophila*. *Cell Discov.* **1**, 15006 (2015).
- Kenmoku, H., Ishikawa, H., Ote, M., Kuraishi, T. & Kurata, S. A subset of neurons controls the permeability of the peritrophic matrix and midgut structure in *Drosophila* adults. *J. Exp. Biol.* **219**, 2331–2339 (2016).
- Jenett, A. et al. A GAL4-driver line resource for *Drosophila* neurobiology. *Cell Rep.* **2**, 991–1001 (2012).
- Kim, A. J., Fenk, L. M., Lyu, C. & Maimon, G. Quantitative predictions orchestrate visual signaling in *Drosophila*. *Cell* **168**, 280–294 e212 (2017).
- Tracey, K. J. Reflex control of immunity. *Nat. Rev. Immunol.* **9**, 418–428 (2009).
- Babcock, D. T., Landry, C. & Galko, M. J. Cytokine signaling mediates UV-induced nociceptive sensitization in *Drosophila* larvae. *Curr. Biol.* **19**, 799–806 (2009).
- Andersen, D. S. et al. The *Drosophila* TNF receptor Grindelwald couples loss of cell polarity and neoplastic growth. *Nature* **522**, 482–486 (2015).
- Kanda, H., Igaki, T., Kanuka, H., Yagi, T. & Miura, M. Wengen, a member of the *Drosophila* tumor necrosis factor receptor superfamily, is required for Eiger signaling. *J. Biol. Chem.* **277**, 28372–28375 (2002).
- Doupe, D. P., Marshall, O. J., Dayton, H., Brand, A. H. & Perrimon, N. *Drosophila* intestinal stem and progenitor cells are major sources and regulators of homeostatic niche signals. *Proc. Natl Acad. Sci. USA* **115**, 12218–12223 (2018).
- Harmansa, S., Alborelli, I., Bieli, D., Caussinus, E. & Affolter, M. A nanobody-based toolset to investigate the role of protein localization and dispersal in *Drosophila*. *eLife* <https://doi.org/10.7554/eLife.22549> (2017).
- Heir, R. & Stellwagen, D. TNF-mediated homeostatic synaptic plasticity: from in vitro to in vivo models. *Front. Cell. Neurosci.* **14**, 565841 (2020).
- Petsakou, A., Sapsis, T. P. & Blau, J. Circadian rhythms in Rho1 activity regulate neuronal plasticity and network hierarchy. *Cell* **162**, 823–835 (2015).
- Ariyapala, I. S. et al. Identification of Split-GAL4 drivers and enhancers that allow regional cell type manipulations of the *Drosophila melanogaster* intestine. *Genetics* **216**, 891–903 (2020).
- Petsakou, A. & Perrimon, N. Bioelectric regulation of intestinal stem cells. *Trends Cell Biol.* <https://doi.org/10.1016/j.tcb.2022.10.003> (2022).
- Harris, M. P. Bioelectric signaling as a unique regulator of development and regeneration. *Development* <https://doi.org/10.1242/dev.180794> (2021).
- Ho, K. Y. L., Khadilkar, R. J., Carr, R. L. & Tanentzapf, G. A gap-junction-mediated, calcium-signaling network controls blood progenitor fate decisions in hematopoiesis. *Curr. Biol.* **31**, 4697–4712 e4696 (2021).
- Dajas-Bailador, F. A., Mogg, A. J. & Wonnacott, S. Intracellular Ca^{2+} signals evoked by stimulation of nicotinic acetylcholine receptors in SH-SY5Y cells: contribution of voltage-operated Ca^{2+} channels and Ca^{2+} stores. *J. Neurochem.* **81**, 606–614 (2002).
- Kim, A. A. et al. Independently paced Ca^{2+} oscillations in progenitor and differentiated cells in an ex vivo epithelial organ. *J. Cell Sci.* <https://doi.org/10.1242/jcs.260249> (2022).

Publisher's note Springer Nature remains neutral with regard to jurisdictional claims in published maps and institutional affiliations.

Springer Nature or its licensor (e.g. a society or other partner) holds exclusive rights to this article under a publishing agreement with the author(s) or other rightsholder(s); author self-archiving of the accepted manuscript version of this article is solely governed by the terms of such publishing agreement and applicable law.

© The Author(s), under exclusive licence to Springer Nature Limited 2023

Article

Methods

Flies were crossed and raised at 19–23 °C with standard fly food. All adult flies were tested 3–5 days after hatching. All experiments were done in female flies. Detailed descriptions of experimental methods are to be found in the Supplementary Information.

Reporting summary

Further information on research design is available in the Nature Portfolio Reporting Summary linked to this article.

Data availability

Reagents are available upon request. The snRNA-seq datasets generated in this work are publicly available in the Gene Expression Omnibus (GEO) database under accession code GSE218641, snRNA-seq dataset of gut from *OreR* female flies during Homeostasis and Recovery. Single-nuclei profiling data from this study can be found at https://www.flyrnai.org/tools/rna_seq_base/web/showProject/39/plot_coord=1/sample_id=all, to allow users to query the expression of any gene of interest. Source data are provided with this paper. All other data are available in figures, Extended Data figures and Supplementary Information files.

Code availability

This study does not use any custom codes for analysis. snRNA-seq datasets were analysed using the standard Seurat pipeline.

Acknowledgements We thank S. Mohr and J. Blau for comments on the manuscript. Confocal imaging was conducted at the MicRoN Facility at Harvard Medical School, and we thank P. Montero Llopis for advice. We thank the Cepko laboratory at Harvard Medical School for sharing their vibratome. We also thank M. Levin for discussions and H. Bellen, G. Tanentzapf, K. O'Connor-Giles, X. Yang, C. Potter, T. R. Lavery, G. Rubin, Janelia FlyLight, DSHB, DRSC/TRiP, VDRC and the Bloomington Stock Center for fly lines, antibodies and reagents. We thank F. Wirtz-Peitz, S. G. Tattikota, R. Binari and H. Li for help in this project, and P. Jouandin, P. Saavedra, L. Lane, D. Doupé, J. Bosch, B. Ewen-Campen, L. Liu, C. Xu, M. R. Riddle and T. Huycke for advice and reagents. We thank C. Villalta and Bestgene for fly injections, H. Elliot and M. Cicconet at the Image and Data Analysis Facility (IDAC), and S. Norrelykke at the Image Analysis Collaboratory (IAC) at Harvard Medical School for advice on Imaris; S. Alon for advice on expansion microscopy; and the Biopolymers Facility and Computing facilities and PCMM Flow Cytometry Facility at Harvard Medical School. All illustrations were created using BioRender.com and publication licences have been obtained. During this study, A.P. was a Good Ventures fellow of the Life Science Research Foundation and next was supported by the Center for the Study of Inflammatory Bowel Disease (grant no. DK043351). N.P. is an investigator of the Howard Hughes Medical Institute. Y.H., Yifang Liu and A.C. were supported by grant no. P41GM132087 and grant no. BBSRC-NSF/BIO (grant no. DBI-2035515). Ying Liu was supported by the Finnish Cultural Foundation.

Author contributions A.P. and N.P. conceptualized the project. A.P. was responsible for the methods, data acquisition, resources, visualization and imaging. A.P. was responsible for the independent replication of experiments at Harvard Medical School. Ying Liu and A.P. performed the FACS analyses. Yifang Liu, Y.H., A.C. and A.P. analysed the single-nuclei data. A.P. wrote the original draft of the manuscript. A.P. and N.P. reviewed, edited and revised the manuscript.

Competing interests The authors declare no competing interests.

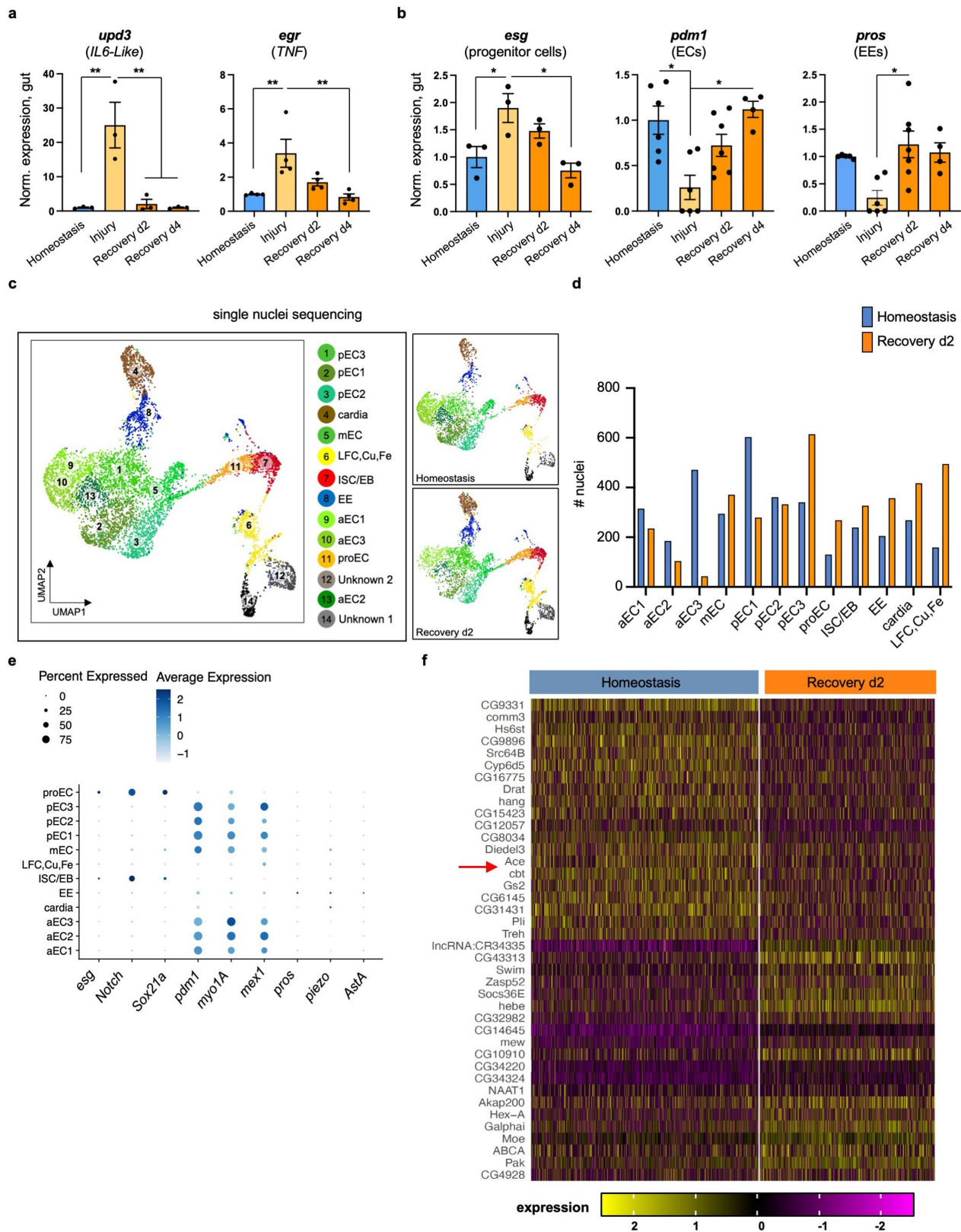
Additional information

Supplementary information The online version contains supplementary material available at <https://doi.org/10.1038/s41586-023-06627-y>.

Correspondence and requests for materials should be addressed to Afroditi Petsakou or Norbert Perrimon.

Peer review information Nature thanks the anonymous reviewers for their contribution to the peer review of this work.

Reprints and permissions information is available at <http://www.nature.com/reprints>.

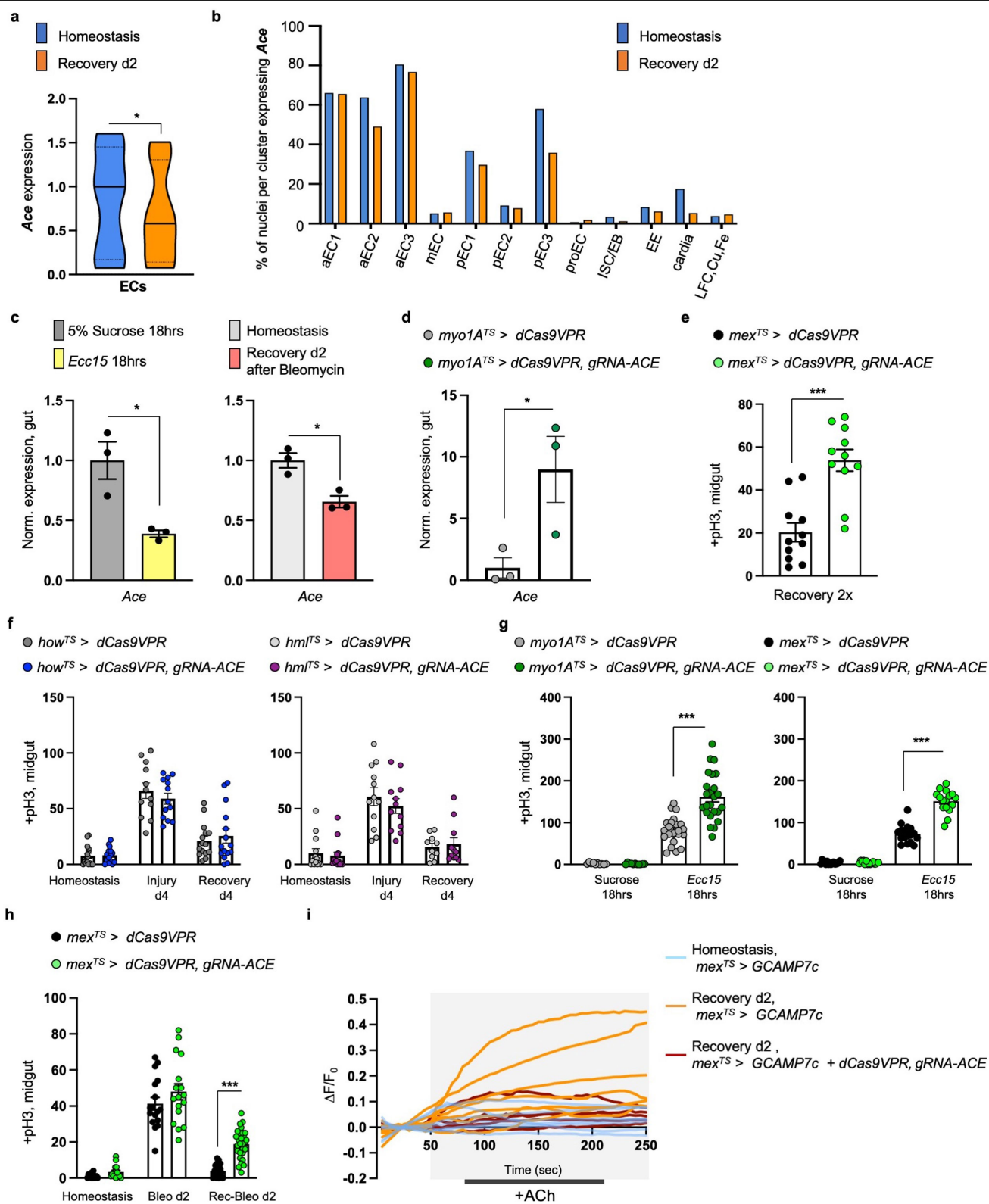


Extended Data Fig. 1 | See next page for caption.

Article

Extended Data Fig. 1 | *Ace* is downregulated during recovery. **a**, Expression levels of conserved inflammatory cytokines (*unpaired-3/upd-3* and *eiger/egr*) in guts of *Ore R* flies undergoing DSS-induced repair. Normalized to Homeostasis. $n = 3$ biologically independent samples per condition. Tukey's one-way Anova: $p = 0.0046$ (*upd3*: Hom. vs Injury & Injury vs Rec. d4), $p = 0.0061$ (*upd3*: Injury vs Rec. d2), $p = 0.0096$ (*egr*: Hom. vs Injury), $p = 0.006$ (Injury vs Rec. d4). **b**, Expression levels of markers for progenitor cells (PCs) (*escargot*, *esg*), ECs (*pdm1*), enteroendocrine cells (EEs) (*prospero*, *pros*) in guts of *Ore R* flies undergoing DSS-induced repair. Normalized to Homeostasis. Homeostasis: $n = 3$ (*esg*), $n = 6$ (*pdm1*), $n = 5$ (*pros*) biologically independent samples. Injury: $n = 3$ (*esg*), $n = 6$ (*pdm1*), $n = 6$ (*pros*) biologically independent samples. Rec. d2: $n = 3$ (*esg*), $n = 7$ (*pdm1*, *pros*) biologically independent samples. Rec. d4: $n = 3$ (*esg*), $n = 4$ (*pdm1*, *pros*) biologically independent samples. Tukey's one-way Anova: $p = 0.0393$ (Hom. vs Injury, *esg*), $p = 0.0112$ (Injury vs Rec. d4, *esg*).

Dunn's Kruskal-Wallis test: $p = 0.0384$ (Hom. vs Injury, *pdm1*), $p = 0.0227$ (Injury vs Rec. 4, *pdm1*), $p = 0.0157$ (Injury vs Rec. d2, *pros*). **c**, Annotated gut cell type clusters of *Ore R* flies after snRNAseq, visualized with UMAP ($n =$ total of 8073 nuclei). **d**, Graph depicting the number of gut nuclei recovered per cluster and per condition after snRNAseq of *Ore R* flies ($n =$ total of 7411 nuclei in gut clusters). **e**, Dot plot per snRNAseq gut cluster illustrating the average expression (blue color range) and percent of expression (dot size) of marker genes for ECs (*pdm1*, *myo1A*, *mex1*), EEs (*pros*, *piezo*, *AstA*) and for PCs (*esg*, *Notch*, *Sox21a*) [PCs: ISC/enteroblast (EB) and proEC]. ($n =$ total of 7411 gut nuclei). **f**, Heatmap of significantly upregulated and downregulated genes in EC clusters (S. Table 1–2) after snRNAseq ($n =$ total of 4547 nuclei in EC clusters). Red arrow: *Acetylcholinesterase (Ace)*. *: $0.05 > p > 0.01$, **: $0.01 > p > 0.001$. Data are presented as mean values \pm SEM.

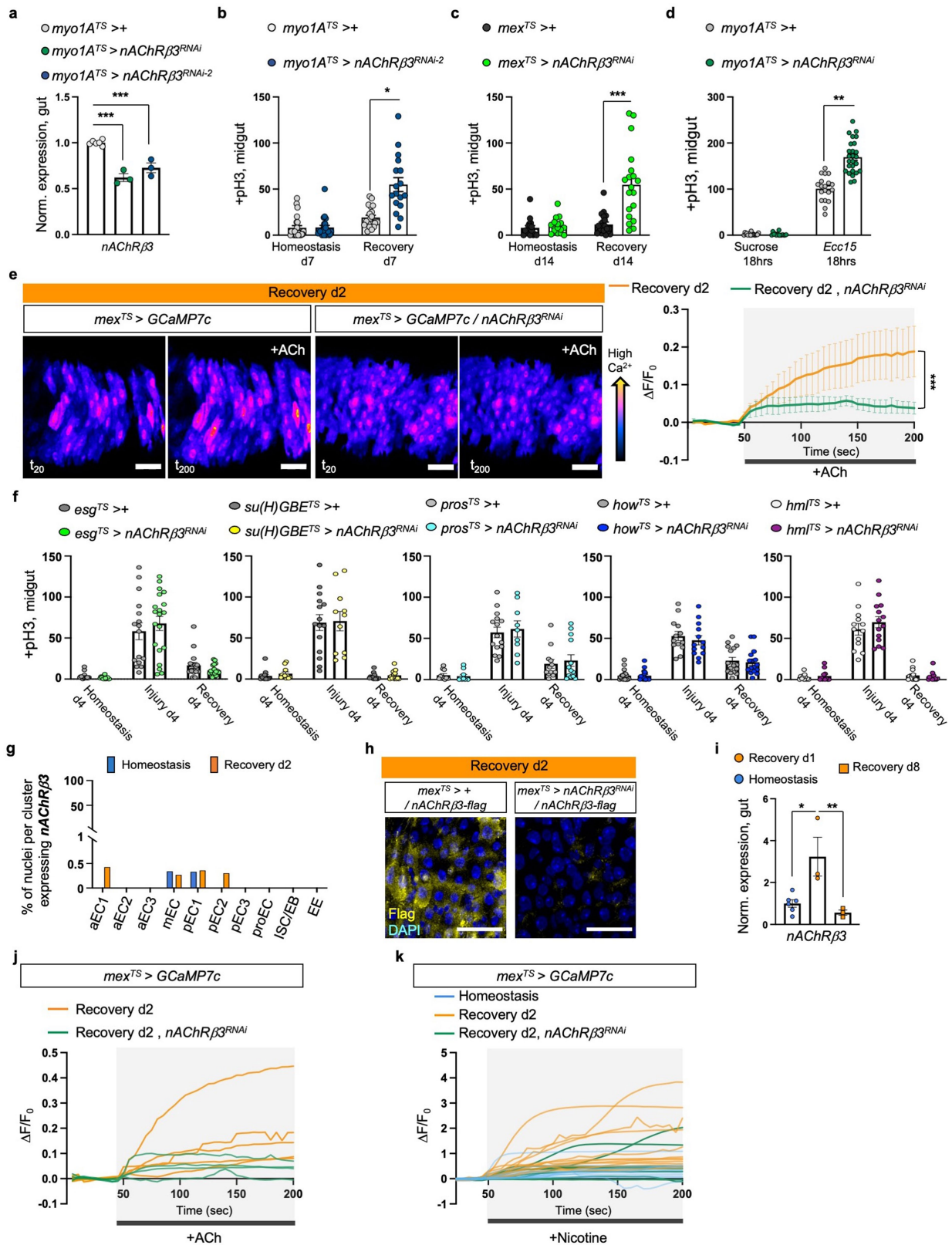


Extended Data Fig. 2 | See next page for caption.

Article

Extended Data Fig. 2 | ACh sensitivity is required for recovery. **a**, Violin plot illustrating the mean expression of *Ace* per condition in EC clusters after snRNAseq of *Ore R* flies ($p = 0.0364$). $n = 4547$ nuclei in EC clusters. Statistics: two-tailed negative binomial exact test, adjusted with Benjamini-Hochberg procedure. Violin plot: median, 1st and 3rd quartile. **b**, Graph depicting percentage of nuclei expressing *Ace* per snRNAseq gut cluster and condition ($n = 7411$ gut nuclei). **c**, Expression levels of *Ace* in *Ore R* guts after 18 h of *Ecc15* bacterial infection (yellow) or 2 days after Bleomycin-injury (pink) compared to unchallenged guts (5% sucrose: grey, homeostasis: light grey). $n = 3$ biologically independent samples per condition. two-tailed t-test: $p = 0.0179$ (Suc. vs *Ecc15*), $p = 0.0121$ (Hom. vs Bleo). **d**, Validation of *ACE* overexpression using CRISPR-OE. $n = 3$ biologically independent samples per genotype. two-tailed t-test: $p = 0.0461$. **e**, Mitotic division counts of proliferating ISCs with anti-pH3 from midgut of control ($mex^{TS} > dCas9VPR$) and flies with conditional *Ace* overexpression ($mex^{TS} > dCas9VPR, gRNA-Ace$) in ECs during Recovery 2x (like Fig. 1f). $n = 11$ guts per genotype examined over 2 independent experiments. two-tailed Mann-Whitney test: $p = 0.0001$. **f**, pH3⁺ counts from midgut of control ($how^{TS} > dCas9VPR, hml^{TS} > dCas9VPR$) and flies with conditional *Ace* overexpression in the visceral muscle ($how^{TS} > dCas9VPR, gRNA-Ace$) and in hemocytes (immune cells, $hml^{TS} > dCas9VPR, gRNA-Ace$). Conditions as Fig. 1e.

Two-way Anova. $how^{TS} > dCas9VPR$: $n = 15$ (Hom, Rec.d4), $n = 12$ (Injury) guts; $how^{TS} > dCas9VPR, gRNA-Ace$: $n = 15$ (Hom, Rec.d4), $n = 13$ (Injury) guts; $hml^{TS} > dCas9VPR$: $n = 13$ (Hom.), $n = 12$ (Injury), $n = 10$ (Rec. d4) guts, $hml^{TS} > dCas9VPR, gRNA-Ace$: $n = 14$ (Hom.), $n = 12$ (Injury), $n = 11$ (Rec. d4) guts, examined over 3 independent experiments. **g**, pH3⁺ counts from midgut of control ($myo1A^{TS} > dCas9VPR, mex^{TS} > dCas9VPR$) and flies with conditional *Ace* overexpression ($myo1A^{TS} > dCas9VPR, gRNA-Ace$ and $mex^{TS} > dCas9VPR, gRNA-Ace$) in ECs after 18hrs of 5% sucrose feeding or 18 h of *Ecc15* oral infection (29 °C). $myo1A^{TS} > dCas9VPR$: $n = 10$ (Suc.), $n = 23$ (*Ecc15*) guts; $myo1A^{TS} > dCas9VPR, gRNA-Ace$: $n = 11$ (Suc.), $n = 24$ (*Ecc15*) guts; $mex^{TS} > dCas9VPR$: $n = 16$ (Suc.), $n = 17$ (*Ecc15*) guts; $mex^{TS} > dCas9VPR, gRNA-Ace$: $n = 15$ (Suc.), $n = 16$ (*Ecc15*) guts, examined over 2 independent experiments. Tukey's one-way Anova. **h**, pH3⁺ counts from $mex^{TS} > dCas9VPR$ and $mex^{TS} > dCas9VPR, gRNA-Ace$ guts during Homeostasis, 2 days feeding with Bleomycin (Bleo d2) and 2 days recovery after Bleomycin (Rec-Bleo d2) at 29 °C. $mex^{TS} > dCas9VPR$: $n = 15$ (Hom.), $n = 17$ (Bleo.), $n = 32$ (Rec.) guts; $mex^{TS} > dCas9VPR, gRNA-Ace$: $n = 16$ (Hom.), $n = 17$ (Bleo.), $n = 29$ (Rec.) guts, examined over 3 independent experiments. Tukey's one-way Anova. **i**, Relative fluorescence intensity ($\Delta F/F_0$) per frame (5 s per frame) and per genotype of individual guts as described in Fig. 1g. *: $0.05 > p > 0.01$, ***: $p < 0.001$. Data are presented as mean values \pm SEM.

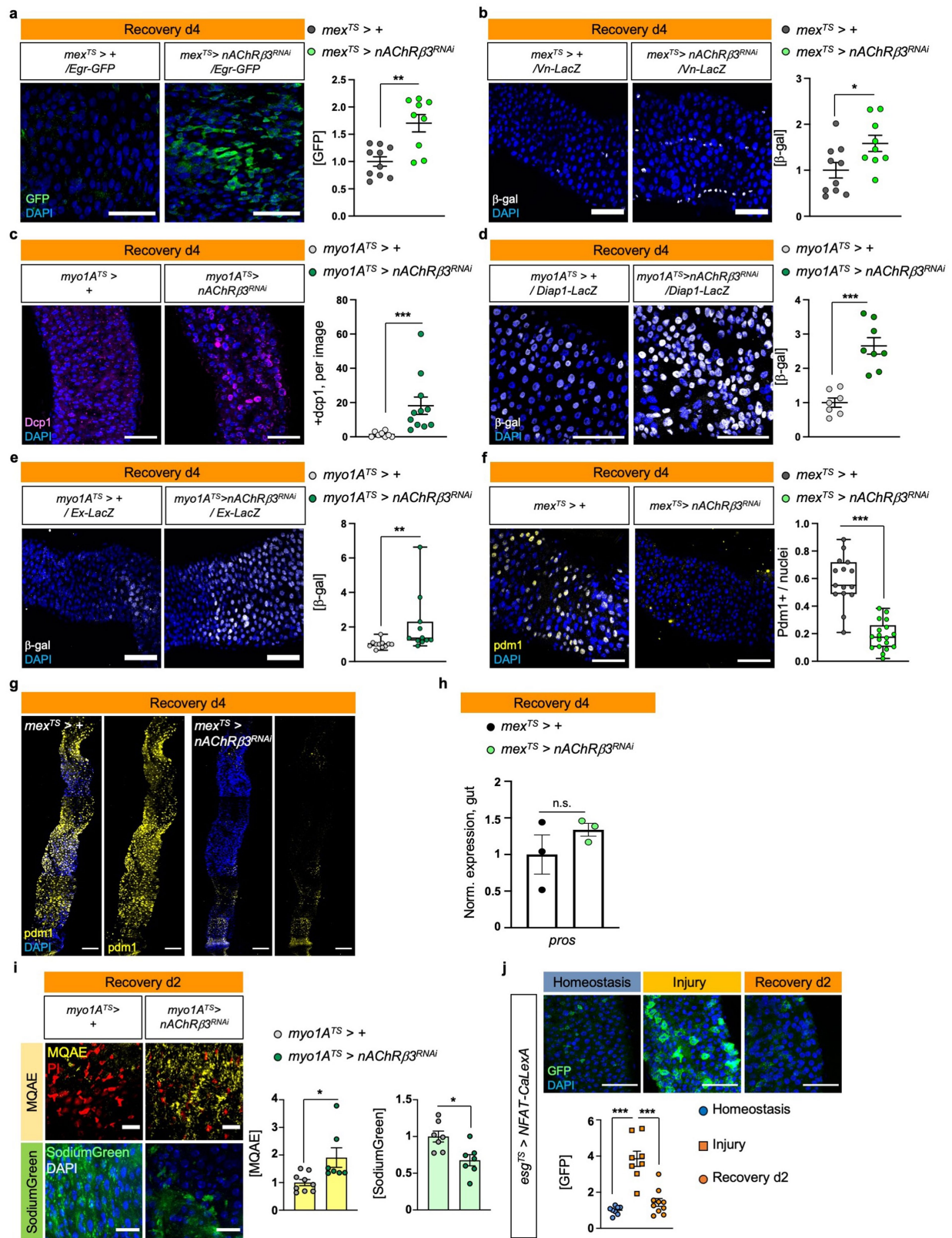


Extended Data Fig. 3 | See next page for caption.

Article

Extended Data Fig. 3 | nAChRβ3 is required in ECs for recovery. **a**, *nAChRβ3^{RNAi}* validation. n = 6 (control), n = 3 (*nAChRβ3^{RNAi}*, *nAChRβ3^{RNAi-2}*) biologically independent samples. Statistics: Dunnett's one-way Anova. **b**, pH3⁺ counts from control (*myoIA^{TS}*+) guts and when *nAChRβ3* is reduced in ECs (*myoIA^{TS}*>*nAChRβ3^{RNAi-2}*). Recovery d7: 7 days standard food (29 °C) after 4 days DSS-feeding (23 °C). Homeostasis d7: 7 days standard food (29 °C). p = 0.0496 (Dunn's Kruskal-Wallis test). *myoIA^{TS}*>+: n = 23 (Hom.), n = 20 (Rec. d7) guts; *myoIA^{TS}*>*nAChRβ3^{RNAi-2}*: n = 23 (Hom.), n = 17 (Rec. d7) guts, examined over 3 independent experiments. **c**, pH3⁺ counts from *mex^{TS}*>+ and *mex^{TS}*>*nAChRβ3^{RNAi}* guts. Recovery d14: 14 days standard food (29 °C) after 4 days of DSS-feeding (23 °C). Homeostasis d14: 14 days standard food (29 °C). p = 0.0007 (Kruskal-Wallis test). *mex^{TS}*>+: n = 16 (Hom.), n = 20 (Rec. d14) guts; *mex^{TS}*>*nAChRβ3^{RNAi}*: n = 16 (Hom.), n = 19 (Rec. d14) examined over 3 independent experiments. **d**, pH3⁺ counts from *myoIA^{TS}*>+ and *myoIA^{TS}*>*nAChRβ3^{RNAi}* guts after *Ecc15* oral infection and after 5% sucrose feeding. Conditions like Extended Data Fig. 2g. p = 0.0099 (Dunn's Kruskal-Wallis test). *myoIA^{TS}*>+: n = 17 (Suc.), n = 19 (*Ecc15*) guts; *myoIA^{TS}*>*nAChRβ3^{RNAi}*: n = 15 (Suc.), n = 26 (*Ecc15*) guts examined over 3 independent experiments. **e**, Representative color-coded sequential frames before (fr₂₀) and after (fr₂₀₀) ACh administration from control (*mex^{TS}*>*GCAM7c*) and *mex^{TS}*>*GCAM7c*+*nAChRβ3^{RNAi}* midguts (as Fig. 1g). scale bar: 25 μm. Accompanying graph: average relative fluorescence intensity (ΔF/F₀) per frame (5 s per frame) and per genotype. n = 4 (control), n = 5 (*nAChRβ3^{RNAi}*) guts examined over 2 independent experiments (two-way Anova). Individual ΔF/F₀ per gut on Extended Data Fig. 3j. **f**, pH3⁺ counts from control and when reducing *nAChRβ3* in progenitor cells (PCs) (*esg^{TS}*>*nAChRβ3^{RNAi}*), enteroblasts (EBs)

(*su(H)GBE^{TS}*>*nAChRβ3^{RNAi}*), enteroendocrine cells (EEs) (*pros^{TS}*>*nAChRβ3^{RNAi}*), visceral muscle (*how^{TS}*>*nAChRβ3^{RNAi}*) and hemocytes (*hml^{TS}*>*nAChRβ3^{RNAi}*). Conditions as Fig. 1e. Statistics: Sidak's two-way Anova. *esg^{TS}*>+: n = 16 (Hom., Injury) n = 17 (Rec.) guts; *esg^{TS}*>*nAChRβ3^{RNAi}*: n = 14 (Hom.), n = 20 (Injury), n = 18 (Rec) guts, over 2 independent experiments. *Su(H)GBE^{TS}*>+: n = 16 (Hom.), n = 15 (Injury), n = 13 (Rec.) guts; *Su(H)GBE^{TS}*>*nAChRβ3^{RNAi}*: n = 11 (Hom., Injury), n = 15 (Rec) guts examined over 2 independent experiments. *pros^{TS}*>+: n = 10 (Hom.), n = 15 (Injury), n = 12 (Rec.) guts; *pros^{TS}*>*nAChRβ3^{RNAi}*: n = 10 (Hom.), n = 9 (Injury), n = 13 (Rec) guts examined over 2 independent experiments. *how^{TS}*>+: n = 20 (Hom.), n = 13 (Injury), n = 16 (Rec.) guts; *how^{TS}*>*nAChRβ3^{RNAi}*: n = 19 (Hom.), n = 13 (Injury), n = 16 (Rec) guts examined over 2 independent experiments. *hml^{TS}*>+: n = 12 (Hom.), n = 13 (Injury), n = 14 (Rec.) guts; *hml^{TS}*>*nAChRβ3^{RNAi}*: n = 12 (Hom.), n = 14 (Injury), n = 13 (Rec) guts examined over 2 independent experiments. **g**, Graph depicting percentage of nuclei expressing *nAChRβ3* per snRNAseq gut cluster (n = 7411 gut nuclei). **h**, *nAChRβ3*-flag validation: Midgut expressing *nAChRβ3*-flag (*mex^{TS}*>+/+/*nAChRβ3-flag*) and when knocking down *nAChRβ3* in ECs (*mex^{TS}*>*nAChRβ3^{RNAi}*/*nAChRβ3-flag*). anti-Flag: *nAChRβ3*-flag (yellow). DAPI: nuclei (blue). Images are representative of 2 independent experiments with similar results. scale bar: 25 μm. **i**, *nAChRβ3* expression levels in *OreR* guts. Tukey's one-way Anova: p = 0.0104 (Hom. vs Rec. d1), p = 0.0085 (Rec. d1 vs Rec. d8). n = 6 (Hom.), n = 3 (Rec. d1, Rec. d8) biologically independent samples. **j-k**, Relative fluorescence intensity (ΔF/F₀) per frame (5 s per frame) and genotype of each gut as described in Extended Data Fig. 3e and Fig. 2g, respectively. *: 0.05 > p > 0.01, **: 0.01 < p < 0.001, ***: p < 0.001. Data are presented as mean values ± SEM.

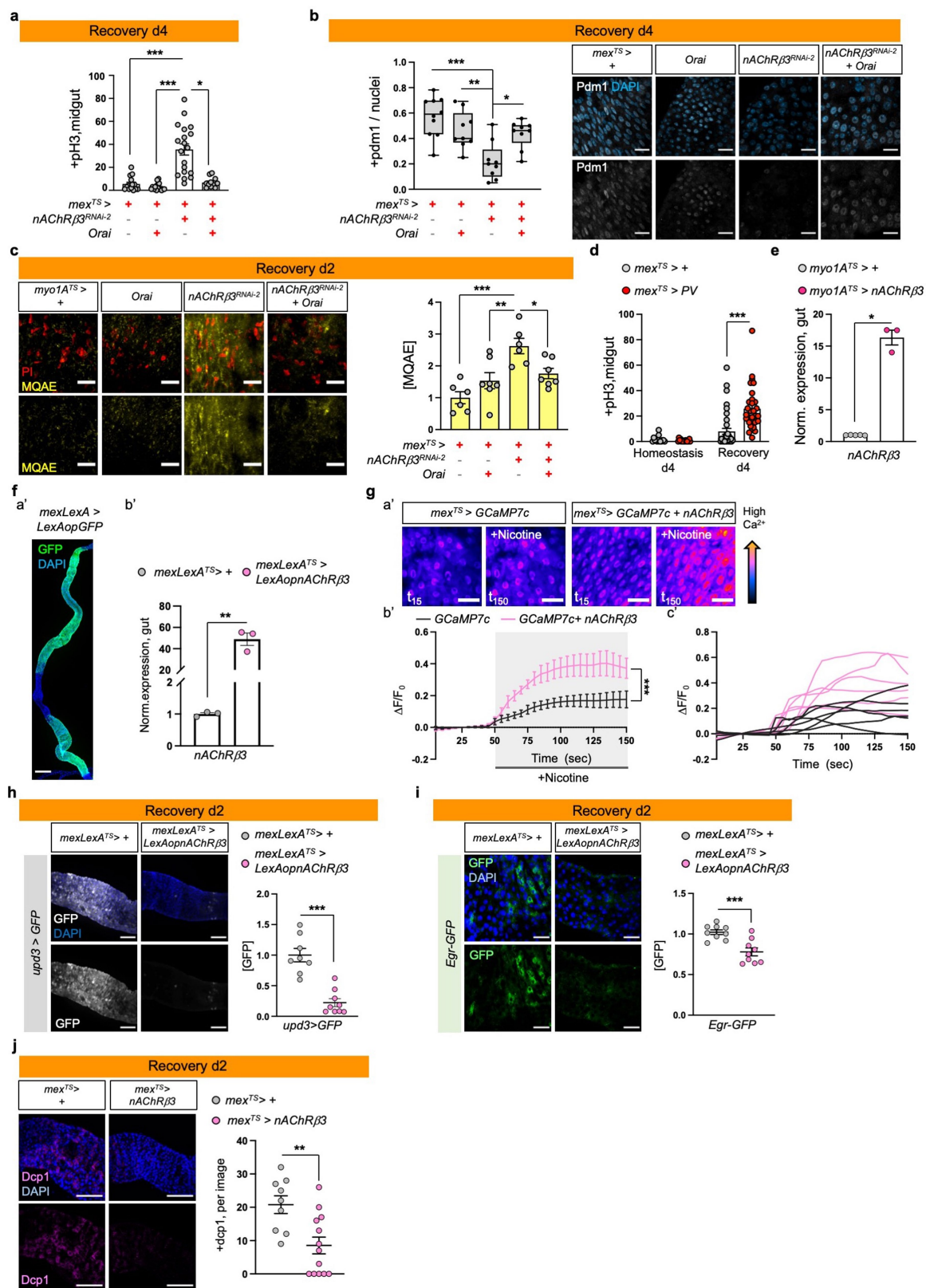


Extended Data Fig. 4 | See next page for caption.

Article

Extended Data Fig. 4 | *nAChRβ3* promotes EC maturation. **a**, Representative image of posterior midgut from control (*mex^{TS}>+/Egr-GFP*) flies and when *nAChRβ3* is reduced in ECs (*mex^{TS}>nAChRβ3^{RNAi}/Egr-GFP*) together with the protein trap Egr-GFP (anti-GFP, green). Accompanying graph: fluorescence fold change per image. n = 10 (control), n = 9 (*nAChRβ3^{RNAi}*) guts examined over 2 independent experiments. Statistics: two-tailed Mann-Whitney test, p = 0.0057. Conditions as Fig. 1e. scale bar: 50 μm. **b**, Representative images of posterior midguts from control (*mex^{TS}>+/Vn-LacZ*) and when *nAChRβ3* is reduced in ECs (*mex^{TS}>nAChRβ3^{RNAi}/Vn-LacZ*) together with the *Vn-LacZ* reporter (anti-β-gal, white). Accompanying graph: fluorescence fold change per image. n = 10 (control), n = 9 (*nAChRβ3^{RNAi}*) guts examined over 2 independent experiments. Conditions as Fig. 1e. Statistics: two-tailed t-test, p = 0.0279. scale bar: 50 μm. **c**, Representative images of posterior midguts from *myo1A^{TS}>+* and *myo1A^{TS}>nAChRβ3^{RNAi}* flies stained with anti-Dcp1: cell death (pink). Conditions as Fig. 1e. Accompanying graph: Dcp1+ cells per image. n = 8 (control), n = 11 (*nAChRβ3^{RNAi}*) guts examined over 2 independent experiments. Statistics: two-tailed Mann-Whitney test. scale bar: 50 μm. **d**, Representative images of posterior midguts from control (*myo1A^{TS}>+/Diap1-LacZ*) and when knocking down *nAChRβ3* in ECs (*myo1A^{TS}>nAChRβ3^{RNAi}/Diap1-LacZ*) together with *Diap1-LacZ* (Yki target gene, anti-β-gal: white). Conditions as Fig. 1e. Accompanying graph: fluorescence fold change per image. n = 7 (control), n = 8 (*nAChRβ3^{RNAi}*) guts examined over 2 independent experiments. Statistics: two-tailed t-test. scale bar: 50 μm. **e**, Representative images of posterior midgut from control (*myo1A^{TS}>+/Ex-LacZ*) and when *nAChRβ3* is reduced in ECs (*myo1A^{TS}>nAChRβ3^{RNAi}/Ex-LacZ*) together with *Ex-LacZ* (Yki target gene, anti-β-gal: white). Conditions

as Fig. 1e. Boxplot: fluorescence fold change per image (median, 1st and 3rd quartile, whiskers: minimum maximum values). n = 11 guts per genotype examined over 2 independent experiments. Statistics: two-tailed Mann-Whitney test, p = 0.0014. scale bar: 50 μm. **f-g**, Representative images from posterior midgut of *mex^{TS}>+* and *mex^{TS}>nAChRβ3^{RNAi}* flies stained with anti-pdm1: EC (yellow). Conditions as Fig. 1e. Boxplot: pdm1+ cells over total nuclei per image (median, 1st and 3rd quartile, whiskers: minimum maximum values). n = 15 (control), n = 18 (*nAChRβ3^{RNAi}*) guts examined over 3 independent experiments. Statistics: two-tailed t-test. scale bars: 50 μm(f), 100 μm(g). **h**, *Pros* expression levels. n = 3 biologically independent samples per genotype. Statistics: two-tailed t-test. **i**, Representative images of posterior midgut assayed with MQAE dye (intracellular Cl⁻ via diffusion-limited collisional quenching, yellow) and SodiumGreen dye (intracellular Na⁺, green) from control *myo1A^{TS}>+* and *myo1A^{TS}>nAChRβ3^{RNAi}* flies. PI: nuclei (Propidium Iodide, red). See Methods for conditions. Accompanying graphs: fluorescence fold change per image. n = 9 (control/MQAE), n = 7 (*nAChRβ3^{RNAi}*/MQAE) guts, n = 7 (SodiumGreen per genotype) guts examined over 2 independent experiments per dye. Statistics: p = 0.0115 (two tailed Mann-Whitney test/ MQAE), p = 0.0103 (two-tailed t-test/SodiumGreen). scale bar: 20 μm. **j**, Representative images from posterior midgut with progenitor cells expressing *NFAT-CaLexA* (*esg^{TS}>NFAT-CaLexA*). anti-GFP: Ca²⁺ (green). *NFAT-CaLexA* was expressed for 2 days (29 °C) per condition. Accompanying graph: fluorescence fold change per image. n = 8 (Hom., Injury), n = 10 (Rec. d2) guts examined over 2 independent experiments (Tukey's one-way Anova). scale bar: 50 μm. *: 0.05 > p > 0.01, **: 0.01 < p < 0.001, ***: p < 0.001. n.s.: non-significant. Data are presented as mean values ± SEM.

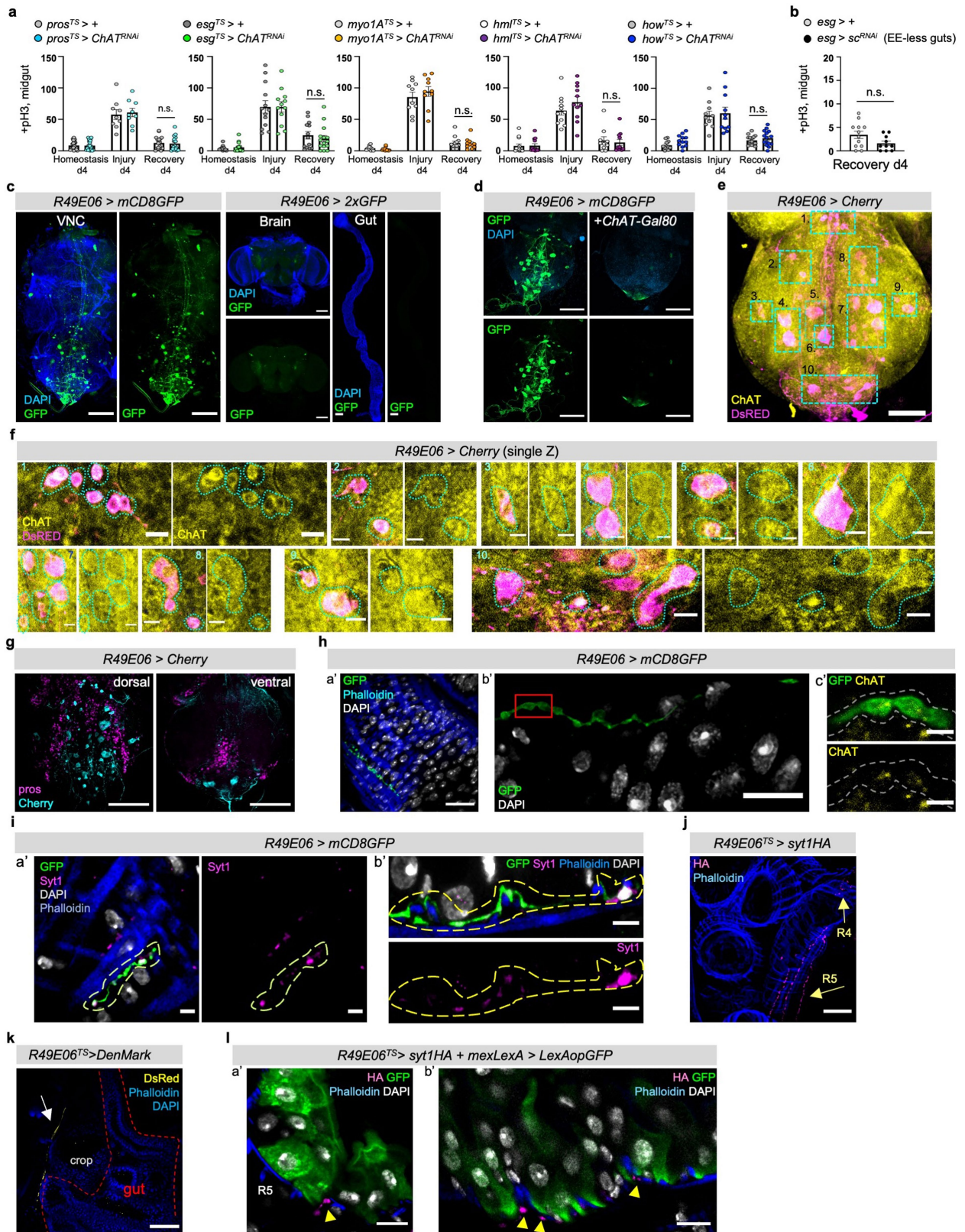


Extended Data Fig. 5 | See next page for caption.

Article

Extended Data Fig. 5 | *nAChRβ3*-mediated Ca^{2+} promotes recovery. a, pH3⁺ counts of control (*mex^{TS}>+*), guts with Orai (Ca^{2+} channel) overexpressed in ECs (*mex^{TS}>Orai*), *nAChRβ3* reduced in ECs (*mex^{TS}>nAChRβ3^{RNAi-2}*) and combined (*mex^{TS}>nAChRβ3^{RNAi-2}+Orai*) during Recovery d4 (as Fig. 1e). n = 15 (*mex^{TS}>+*), n = 19 (*mex^{TS}>nAChRβ3^{RNAi-2}*), n = 16 (*mex^{TS}>Orai*), n = 11 (*mex^{TS}>nAChRβ3^{RNAi-2}+Orai*) guts examined over 2 independent experiments. Statistics: Dunn's Kruskal-Wallis test, p = 0.013 (*nAChRβ3^{RNAi-2}* vs *nAChRβ3^{RNAi-2}+Orai*). **b**, Representative images of posterior midgut of flies as in Extended Data Fig. 5a. anti-pdm1: ECs (grey). Boxplot: pdm1+ cells over total nuclei per image (median, 1st and 3rd quartile, whiskers: minimum maximum values). n = 10 (control), n = 9 (*nAChRβ3^{RNAi-2}*, *Orai nAChRβ3^{RNAi-2}+Orai* guts) examined over 2 independent experiments. Statistics: Tukey's one-way Anova, p = 0.0048 (*nAChRβ3^{RNAi-2}* vs *Orai*), p = 0.0144 (*nAChRβ3^{RNAi-2}* vs *nAChRβ3^{RNAi-2}+Orai*). scale bar: 25 μm. **c**, Representative images of posterior midguts assayed with MQAE (like Extended Data Fig. 4i) of *myo1A^{TS}>+*, *myo1A^{TS}>Orai*, *myo1A^{TS}>nAChRβ3^{RNAi-2}* and *myo1A^{TS}>nAChRβ3^{RNAi-2}+Orai* flies. Accompanying graph: fluorescence fold change per image. n = 6 (*myo1A^{TS}>+*), n = 6 (*myo1A^{TS}>nAChRβ3^{RNAi-2}*), n = 7 (*myo1A^{TS}>Orai*), n = 7 (*myo1A^{TS}>nAChRβ3^{RNAi-2}+Orai*) guts examined over 2 independent experiments. Statistics: Tukey's one-way Anova, p = 0.0002 (control vs *nAChRβ3^{RNAi-2}*), p = 0.0084 (*Orai* vs *nAChRβ3^{RNAi-2}*), p = 0.0441 (*nAChRβ3^{RNAi-2}* vs *Orai + nAChRβ3^{RNAi-2}*). scale bar: 25 μm. **d**, pH3⁺ counts from control (*mex^{TS}>+*) and flies overexpressing parvalbumin in ECs (*mex^{TS}>PV*). Conditions as Fig. 1e. Control: n = 14 (Hom.), n = 37 (Rec.d4) guts, *mex^{TS}>PV*: n = 17 (Hom.), n = 30 (Rec.d4) guts examined over 3 independent experiments. Statistics: Dunn's Kruskal-Wallis test. **e**, Validation of UAS-*nAChRβ3*. n = 6 (control), n = 3 (*myo1A^{TS}>nAChRβ3*) biologically independent samples. Statistics: two-tailed Mann-Whitney test, p = 0.0357. **f**, Validation of a': *mexLexA*

(*mexLexA::GAD*), scale bar: 200 μm. Image is representative of 2 independent experiments with similar results; b': *LexAopnAChRβ3*. n = 3 biologically independent samples per genotype. Statistics: two-tailed t-test, p = 0.0012. **g**, a': Representative color-coded sequential frames of *mex^{TS}>GCAM7c* and *mex^{TS}>GCAM7c+nAChRβ3* guts before (t₁₅) and after (t₁₅₀) nicotine administration. b': average relative fluorescence intensity ($\Delta F/F_0$) per frame (5 s per frame) and genotype. Conditions: 2 days standard food (29 °C). N = 6 guts per genotype examined over 2 independent experiments. c': relative fluorescence intensity of each gut. Statistics: two-way Anova. scale bar: 25 μm. **h**, Representative images of posterior midguts from control (*mexLexA^{TS}>+/upd3>GFP*) and when *nAChRβ3* is overexpressed in ECs (*mexLexA^{TS}>LexAopnAChRβ3/upd3>GFP*) together with *upd3-Gal4* driving *UAS-GFP* (anti-GFP, white). Conditions as Fig. 3g. Accompanying graph: fluorescence fold change per image. n = 8 (control), n = 9 (*mexLexA^{TS}>LexAopnAChRβ3*) guts examined over 2 independent experiments. Statistics: two-tailed Mann-Whitney test, p = 0.0002. scale bar: 100 μm. **i**, Representative images of posterior midguts from *mexLexA^{TS}>+/Egr-GFP* and *mexLexA^{TS}>LexAopnAChRβ3/Egr-GFP* flies (anti-GFP, green). Conditions as Fig. 3g. Accompanying graph: fluorescence fold change per image. n = 9 guts per genotype examined over 2 independent experiments. Statistics: two-tailed t-test, p = 0.0006. scale bar: 25 μm. **j**, Representative images of posterior midguts from control (*mex^{TS}>+*) and *mex^{TS}>nAChRβ3* flies stained with anti-Dcp1 (pink). Conditions like Fig. 3g. Accompanying graph: Dcp1+ cells per image. n = 9 (control), n = 13 (*mex^{TS}>nAChRβ3*) guts per genotype examined over 2 independent experiments. Statistics: two-tailed Mann-Whitney test, p = 0.0064. scale bar: 100 μm. DAPI: nuclei (blue). PI: nuclei (Propidium iodide, red). *: 0.05 > p > 0.01, **: 0.01 < p < 0.001, ***: p < 0.001. Data are presented as mean values ± SEM.

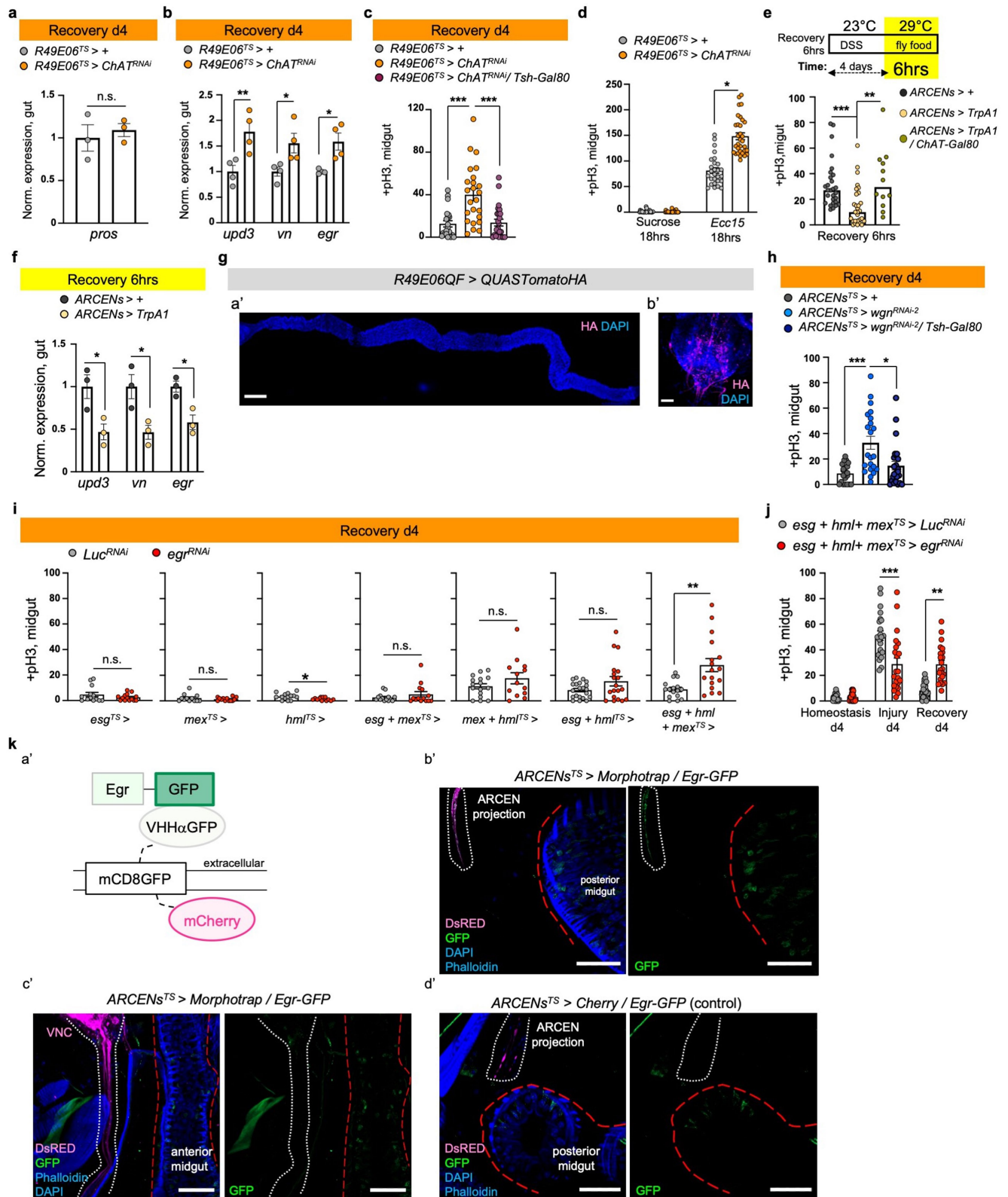


Extended Data Fig. 6 | See next page for caption.

Article

Extended Data Fig. 6 | R49E06-neurons innervate the gut. **a**, pH3⁺ counts from control and from flies with conditional reduction of *ChAT* (*Choline Acetyltransferase*) in enteroendocrine cells (EEs) (*pros^{TS}>*), progenitor cells (PCs) (*esg^{TS}>*), ECs (*myoIA^{TS}>*), hemocytes (*hml^{TS}>*), visceral muscle (*how^{TS}>*). Conditions as Fig. 1e. *pros^{TS}>*; n = 20 (Hom.), n = 9 (Injury), n = 18 (Rec.) guts; *pros^{TS}>ChAT^{RNAi}*; n = 20 (Hom.), n = 9 (Injury), n = 16 (Rec.) guts; *esg^{TS}>*; n = 13 (per condition) guts; *esg^{TS}>ChAT^{RNAi}*; n = 15 (Hom.), n = 12 (Injury), n = 15 (Rec.) guts; *myoIA^{TS}>*; n = 11 (Hom.), n = 10 (Injury), n = 12 (Rec.) guts; *myoIA^{TS}>ChAT^{RNAi}*; n = 12 (Hom.), n = 10 (Injury), n = 11 (Rec.) guts; *hml^{TS}>*; n = 13 (Hom.), n = 11 (Injury), n = 10 (Rec.) guts; *hml^{TS}>ChAT^{RNAi}*; n = 12 (Hom.), n = 11 (Injury), n = 11 (Rec.) guts; *how^{TS}>*; n = 11 (Hom.), n = 10 (Injury), n = 15 (Rec.) guts; *how^{TS}>ChAT^{RNAi}*; n = 12 (Hom.), n = 11 (Injury), n = 15 (Rec.) guts examined over two independent experiments per cell type. Statistics: Sidak's two-way Anova. **b**, pH3⁺ counts from control (*esg>+*) and from flies without EEs (*esg>sc^{RNAi}*). n = 12 (control), n = 10 (*esg>sc^{RNAi}*) guts examined over 2 independent experiments. Statistics: two-tailed t-test. **c**, VNC (adult Ventral Nerve Cord), brain, and gut from *R49E06>mCD8GFP* and *R49E06>2xEGFP* flies. Images are representative of 3 independent experiments with similar results. anti-GFP: green. scale bar: 100 μ m. **d**, Posterior VNC from *R49E06>mCD8GFP* flies and together with the cholinergic repressor *R49E06>mCD8GFP/ChAT-Gal80*. anti-GFP: green. scale bar: 100 μ m. Images are representative of 2 independent experiments with similar results. **e-f**, Z-stack (e) and single Z-planes (f) from posterior VNC of *R49E06>6xmCherry*. anti-DsRed: magenta, anti-ChAT: yellow, numbered squares: ChAT+R49E06-neurons. scale bar: 50 μ m (e), 10 μ m (f). Image (e) is representative of 2 independent experiments

with similar results. **g**, Posterior VNC from *R49E06>6xmCherry*. anti-pros: magenta, anti-DsRed: cyan. Ventral and dorsal from same stack. scale bar: 100 μ m. Images are representative of 2 independent experiments with similar results. **h**, R49E06-innervations (anti-GFP, green) in midguts of *R49E06>mCD8GFP* flies; a': R4, Homeostasis, b': R5, Recovery d2. Red square: domain of R49E06-innervation in c. c': R49E06-innervation (grey line), anti-ChAT: yellow. scale bar: 20 μ m (h-a'), 10 μ m (h-b'), 2 μ m (h-c'). Images are representative of 2 independent experiments with similar results per condition. **i**, a': innervated R4, b': R5 from *R49E06>mCD8GFP* flies during Homeostasis. anti-GFP: R49E06-innervations (green), anti-Syt1: synaptic-vesicle marker (magenta). Yellow dots: Syt1+ boutons across innervations. scale bar: 4 μ m. Images are representative of 2 independent experiments with similar results. **j**, *R49E06^{TS}>syt1HA* fly abdomen during Recovery d2. Yellow arrows: R49E06-innervations (anti-HA, magenta). scale bar: 50 μ m. Images are representative of 3 independent experiments with similar results. **k**, Fly abdomen with DenMark expressed in R49E06-projections (*R49E06^{TS}>DenMark*) during Recovery d2 (as Fig. 4a). anti-DsRed: DenMark (yellow). White arrow: DenMark-expressing ARCEN-projections, Dotted red line: gut. scale bar: 100 μ m. Images are representative of 2 independent experiments with similar results. **l**, R5 from *R49E06^{TS}>syt1HA+mexLexA>6xLexAopGFP* (a') and *R49E06^{TS}>syt1HA+mexLexA>LexAopGFP* (b') flies during Recovery d2. Yellow arrowheads: R49E06-innervations carrying the presynaptic marker syt1HA (anti-HA, magenta) near ECs (anti-GFP, green). Images are representative of 3 independent experiments with similar results. scale bar: 10 μ m. Phalloidin: muscle (blue). DAPI: nuclei (blue or white); n.s.: non-significant. Data are presented as mean values \pm SEM.

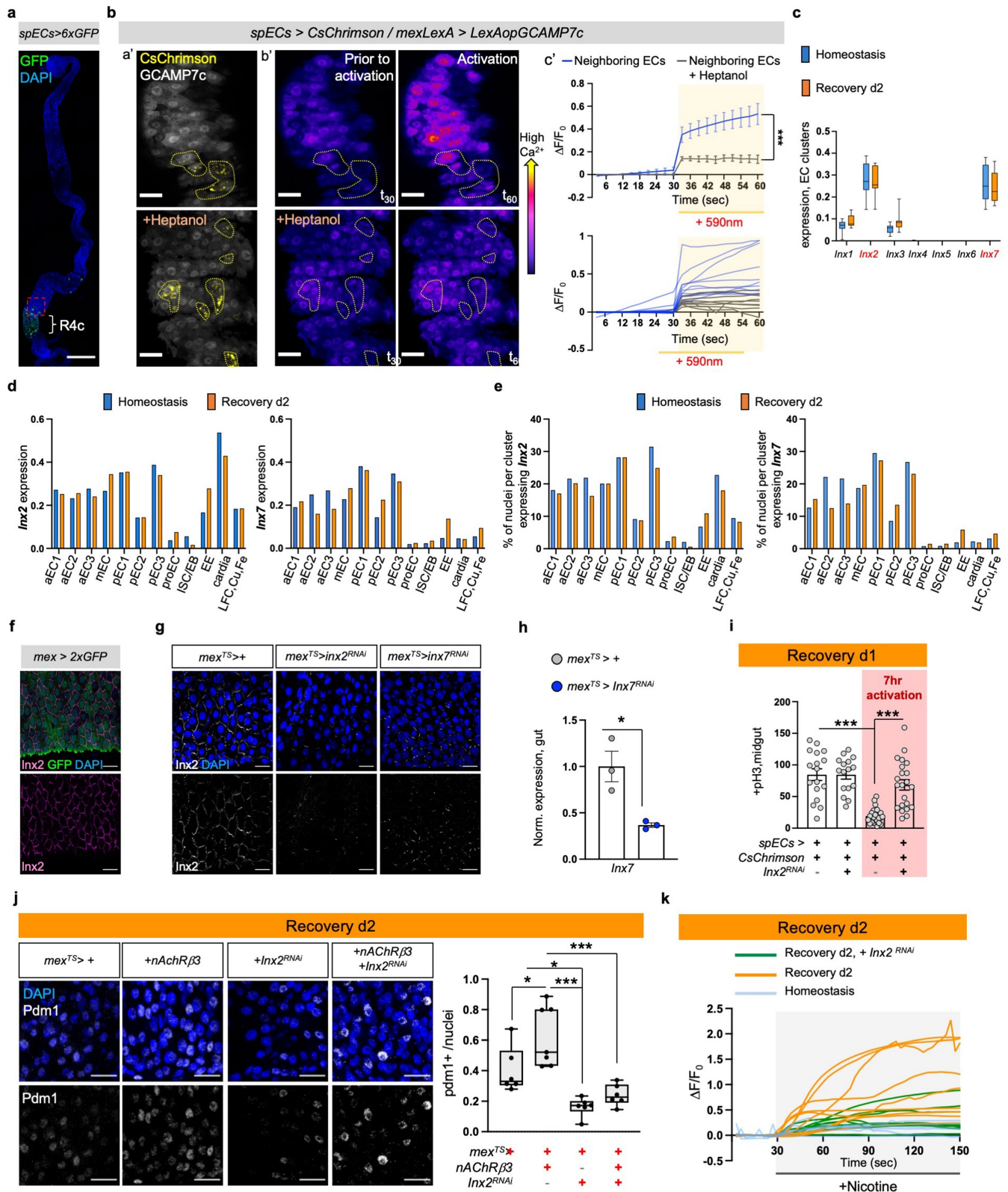


Extended Data Fig. 7 | See next page for caption.

Article

Extended Data Fig. 7 | Egr-ARCEs signaling promotes recovery. a-b, Pros, *upd3*, *vn*, *egr* expression levels from control (*R49E06^{TS}>+*) guts and guts after knocking down *ChAT* in *R49E06*-neurons (*R49E06^{TS}>ChAT^{RNAi}*). Conditions as Fig. 1e. a: n = 3 biologically independent samples. b: n = 4 biologically independent samples. Normalized to *R49E06^{TS}>+*. Statistics: (a) two-tailed t-test, (b) Sidak's two-way Anova: p = 0.0038 (*upd3*), p = 0.0412 (*vn*), p = 0.0298 (*egr*). c, pH3⁺ counts from *R49E06^{TS}>+* (control), *R49E06^{TS}>ChAT^{RNAi}* flies and flies co-expressing the VNC repressor (*R49E06^{TS}>ChAT^{RNAi}/Tsh-Gal80*). n = 21 (control), n = 24 (*R49E06^{TS}>ChAT^{RNAi}*, *R49E06^{TS}>ChAT^{RNAi}/Tsh-Gal80*) guts examined over 3 independent experiments. Statistics: Dunn's Kruskal-Wallis test: p = 0.0004. Conditions as Fig. 1e. d, pH3⁺ counts from *R49E06^{TS}>+* and *R49E06^{TS}>ChAT^{RNAi}* flies after oral *Ecc15* infection or 5% sucrose feeding (as Extended Data Fig. 2g). n = 27 (*R49E06^{TS}>+* per condition), n = 24 (*R49E06^{TS}>ChAT^{RNAi}*, sucrose), n = 32 (*R49E06^{TS}>ChAT^{RNAi}*, *Ecc15*) guts examined over 3 independent experiments. Statistics: Dunn's Kruskal-Wallis test: p = 0.013. e, Experimental schematic and pH3⁺ counts, from control (*ARCENs>+*) flies, flies with 6 h thermo-activation of ARCEs with the *TrpA1* channel (*ARCENs>TrpA1*) and when cholinergic neurons are inhibited (*ARCENs>TrpA1/ChAT-Gal80*). n = 28 (control), n = 29 (*ARCENs>TrpA1*), n = 12 (*ARCENs>TrpA1/ChAT-Gal80*) guts examined over 2 independent experiments. Dunn's Kruskal-Wallis test: p = 0.0005 (control vs *TrpA1*), p = 0.0069 (*TrpA1* vs *TrpA1/ChAT-Gal80*). f, *upd3*, *vn*, *egr* expression levels from *ARCENs>+* (control) and *ARCENs>TrpA1* guts. Conditions as Extended Data Fig. 7e. n = 3 biologically independent samples per genotype. Normalized to *ARCENs>+*. Sidak's two-way Anova: p = 0.0114 (*upd3*), p = 0.0109 (*vn*), p = 0.0461 (*egr*). g, Validation of *R49E06QF*. a': gut (scale bar: 200 μm), b': posterior VNC (scale bar 50 μm). Images are representative of 2 independent experiments with similar results. h, pH3⁺ counts from control (*ARCENs^{TS}>+*) flies, flies with TNF receptor *wgn* reduced in ARECNS (*ARCENs^{TS}>wgn^{RNAi-2}*) and flies co-expressing the VNC repressor (*ARCENs^{TS}>wgn^{RNAi-2}/Tsh-Gal80*). Conditions as Fig. 1e. n = 21 (control), n = 22 (*ARCENs^{TS}>*

wgn^{RNAi-2}), n = 25 (*ARCENs^{TS}>wgn^{RNAi-2}/Tsh-Gal80*) guts examined over 3 independent experiments. Dunn's Kruskal-Wallis: p = 0.0004 (control vs *wgn^{RNAi-2}*), p = 0.0105 (*wgn^{RNAi-2}* vs *wgn^{RNAi-2}/Tsh-Gal80*). i, pH3⁺ from control (*Luc^{RNAi}*) and flies with *egr* reduced (*egr^{RNAi}*) in progenitor cells (PCs) (*esg^{TS}>*), ECs (*mex^{TS}>*) and hemocytes (*hml^{TS}>*). Conditions as Fig. 1e. *esg^{TS}*: n = 13 (control), n = 14 (*egr^{RNAi}*) guts examined over 2 independent experiments (two-tailed Mann-Whitney test). *mex^{TS}*: n = 12 (control), n = 13 (*egr^{RNAi}*) guts examined over 2 independent experiments (two-tailed Mann-Whitney test). *hml^{TS}*: n = 14 (control), n = 13 (*egr^{RNAi}*) guts examined over 2 independent experiments (two-tailed Mann-Whitney test, p = 0.028). *esg+mex^{TS}*: n = 14 guts per genotype examined over 2 independent experiments (two-tailed Mann-Whitney test). *mex+hml^{TS}*: n = 16 (control), n = 13 (*egr^{RNAi}*) guts examined over 2 independent experiments (two-tailed t-test). *esg+hml^{TS}*: n = 21 (control), n = 19 (*egr^{RNAi}*) guts examined over 3 independent experiments (two-tailed Mann-Whitney test). *esg+mex+hml^{TS}*: n = 16 (control), n = 19 (*egr^{RNAi}*) guts examined over 3 independent experiments (two-tailed Mann-Whitney test). j, pH3⁺ counts from *esg+hml+mex^{TS}>Luc^{RNAi}* (control) and *esg+hml+mex^{TS}>egr^{RNAi}* flies. Conditions as Fig. 1e. control: n = 23 (Hom.), n = 22 (Injury), n = 40 (Rec.) guts; *egr^{RNAi}*: n = 24 (Hom.), n = 22 (Injury), n = 39 (Rec.) guts examined over 3 independent experiments. Statistics: Sidak's two-way Anova. k, a': Schematic of Egr-GFP bound to extracellular morphotrap (VHHaGFP). b'-d': Images from the abdomen (b', d') and thorax (c') of flies expressing the morphotrap in ARCEs while expressing Egr-GFP (*ARCENs^{TS}>morphotrap/Egr-GFP*) and of control flies without the morphotrap (*ARCENs^{TS}>Cherry/Egr-GFP*). white dotted lines: ARCE projections. red lines: midgut (b', d': posterior, c': anterior). Sectioning as Fig. 4a. anti-DsRed: Morphotrap and Cherry (magenta). Anti-GFP: Egr (green), Phalloidin: muscle (blue), DAPI: nuclei (blue). Images are representative of 2 independent experiments with similar results. scale bar 50 μm. n.s.: non-significant, *: 0.05 > p > 0.01, **: 0.01 < p < 0.001, ***: p < 0.001. Data are presented as mean values ± SEM.

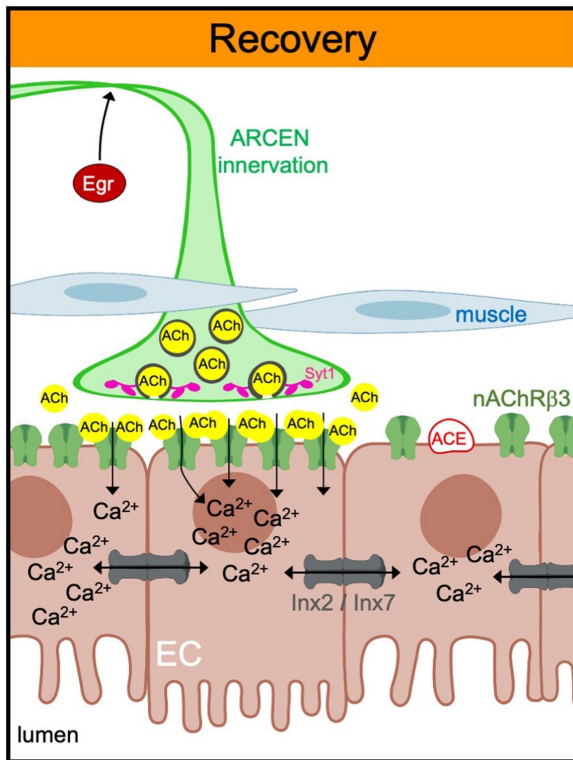


Extended Data Fig. 8 | See next page for caption.

Article

Extended Data Fig. 8 | Ca^{2+} spreads in ECs via gap junctions. **a**, Gut image with a subpopulation of ECs (spECs) expressing GFP (*spECs > 6xGFP*) that are located in R4c (between R4 and R5). anti-GFP: green. Red dotted square: area imaged in Extended Data Fig. 8b. scale bar 100 μm . Image is representative of 2 independent experiments with similar results. **b**, **a'**: Posterior midgut images of flies expressing *CsChrimson* in spECs (*spEC > CsChrimson*, yellow) while expressing *GCAMP7c* in all ECs (*mexLexA > LexAopGCAMP7c*, grey). **b'**: Color-coded sequential frames from *spEC > CsChrimson + mexLexA > LexAopGCAMP7c* gut prior (t_{30}) and during (t_{60}) *CsChrimson*-activation. Lower panels: Heptanol addition (gap junction blocker). **c'**: Fluorescence intensity ($\Delta F/F_0$) of neighboring ECs (non-expressing *CsChrimson*) per frame ($\sim 3 \text{ sec/frame}$) per condition. Upper graph: average $\Delta F/F_0$ per condition. Lower graph: individual $\Delta F/F_0$ per gut. $n = 10$ (Neighboring ECs), $n = 9$ (Neighboring ECs+Heptanol) guts examined over 3 independent experiments. Statistics: two-way Anova. yellow dots: *CsChrimson*-expressing ECs (spECs). scale bar 20 μm . **c**, Mean expression of each *Innexin* (gap junction components) in all snRNAseq EC clusters per condition ($n = 4547$ nuclei in EC clusters). Boxplot: median, 1st and 3rd quartile, whiskers: minimum maximum values. **d**, Graph depicting *Inx2* and *Inx7* mean expression per snRNAseq gut cluster and condition ($n = 7411$ gut nuclei). **e**, Graph depicting the percentage of nuclei expressing *Inx7* and *Inx2* per snRNAseq gut cluster and condition ($n = 7411$ gut nuclei). **f**, Posterior midgut expressing GFP in ECs (*mex > 2xGFP*). anti-GFP: green, anti-*Inx2*: magenta. scale bar 20 μm . Image is representative of 2 independent experiments with

similar results. **g**, Posterior midgut of control (*mex^{TS} > +*), and when conditionally knocking down *Inx2* and *Inx7* in ECs (*mex^{TS} > Inx2^{RNAi}* and *mex^{TS} > Inx7^{RNAi}*). Conditions: 2 days standard food (29 °C). anti-*Inx2*: grey. Images are representative of 2 independent experiments with similar results. scale bar 20 μm . **h**, Validation of *Inx7* RNAi. $n = 3$ biologically independent samples per genotype. Statistics: two-tailed t-test ($p = 0.0188$). **i**, pH3⁺ counts from *spECs > CsChrimson* and *spECs > CsChrimson + Inx2^{RNAi}* flies without or with 7hr opto-activation (red square) during Recovery d1. No light: $n = 17$ (*spECs > CsChrimson*), $n = 18$ (*spECs > CsChrimson + Inx2^{RNAi}*) guts; Red light: $n = 18$ (*spECs > CsChrimson*), $n = 22$ (*spECs > CsChrimson + Inx2^{RNAi}*) guts, examined over 3 independent experiments (Tukey's two-way Anova). **j**, Posterior midgut images from *mex^{TS} > +*, *mex^{TS} > nAcR β 3*, *mex^{TS} > Inx2^{RNAi}* and *mex^{TS} > nAcR β 3 + Inx2^{RNAi}* flies. scale bar 20 μm . Conditions as Fig. 5f. anti-pdm1: ECs (grey). Accompanying boxplot: pdm1+ ratio (median, 1st and 3rd quartile, whiskers: minimum maximum values). $n = 7$ (*mex^{TS} > nAcR β 3*), $n = 6$ (*mex^{TS} > +*, *mex^{TS} > Inx2^{RNAi}*, *mex^{TS} > nAcR β 3 + Inx2^{RNAi}*) guts, examined over 2 independent experiments. Tukey's two-way Anova: $p = 0.0392$ (*mex^{TS} > +* vs *mex^{TS} > nAcR β 3*), $p = 0.0307$ (*mex^{TS} > +* vs *mex^{TS} > Inx2^{RNAi}*), $p = 0.0003$ (*mex^{TS} > nAcR β 3* vs *mex^{TS} > nAcR β 3 + Inx2^{RNAi}*). **k**, Relative fluorescence intensity ($\Delta F/F_0$) per frame (3 s per frame) per genotype and per condition of individual guts as described in Fig. 5g. $n = 6$ (Hom.), $n = 9$ (Rec.), $n = 8$ (*Inx2^{RNAi}*) guts examined over 2 independent experiments. DAPI: blue (nuclei). *: $0.05 > p > 0.01$, **: $0.01 > p < 0.001$, ***: $p < 0.001$. Data are presented as mean values \pm SEM.



Extended Data Fig. 9 | ARCENs trigger nAChRβ3-mediated Ca^{2+} currents in ECs to promote intestinal epithelial recovery after injury. Model: During recovery, ECs become sensitive (*Ace* reduction) and receptive (nAChRβ3 increase) to ACh while ARCEN-innervations strengthen their Syt1+ boutons in an Egr-dependent manner. Cholinergic signaling from ARCENs to ECs triggers nAChR-mediated Ca^{2+} currents that propagate across more ECs via Inx2–Inx7 gap junctions to advance EC maturation, ion balance and transition to homeostasis. Illustration generated with BioRender.com.

Reporting Summary

Nature Portfolio wishes to improve the reproducibility of the work that we publish. This form provides structure for consistency and transparency in reporting. For further information on Nature Portfolio policies, see our [Editorial Policies](#) and the [Editorial Policy Checklist](#).

Statistics

For all statistical analyses, confirm that the following items are present in the figure legend, table legend, main text, or Methods section.

n/a Confirmed

- | | | |
|-------------------------------------|-------------------------------------|--|
| <input type="checkbox"/> | <input checked="" type="checkbox"/> | The exact sample size (n) for each experimental group/condition, given as a discrete number and unit of measurement |
| <input type="checkbox"/> | <input checked="" type="checkbox"/> | A statement on whether measurements were taken from distinct samples or whether the same sample was measured repeatedly |
| <input type="checkbox"/> | <input checked="" type="checkbox"/> | The statistical test(s) used AND whether they are one- or two-sided
<i>Only common tests should be described solely by name; describe more complex techniques in the Methods section.</i> |
| <input checked="" type="checkbox"/> | <input type="checkbox"/> | A description of all covariates tested |
| <input type="checkbox"/> | <input checked="" type="checkbox"/> | A description of any assumptions or corrections, such as tests of normality and adjustment for multiple comparisons |
| <input type="checkbox"/> | <input checked="" type="checkbox"/> | A full description of the statistical parameters including central tendency (e.g. means) or other basic estimates (e.g. regression coefficient) AND variation (e.g. standard deviation) or associated estimates of uncertainty (e.g. confidence intervals) |
| <input type="checkbox"/> | <input checked="" type="checkbox"/> | For null hypothesis testing, the test statistic (e.g. F , t , r) with confidence intervals, effect sizes, degrees of freedom and P value noted
<i>Give P values as exact values whenever suitable.</i> |
| <input checked="" type="checkbox"/> | <input type="checkbox"/> | For Bayesian analysis, information on the choice of priors and Markov chain Monte Carlo settings |
| <input checked="" type="checkbox"/> | <input type="checkbox"/> | For hierarchical and complex designs, identification of the appropriate level for tests and full reporting of outcomes |
| <input checked="" type="checkbox"/> | <input type="checkbox"/> | Estimates of effect sizes (e.g. Cohen's d , Pearson's r), indicating how they were calculated |

Our web collection on [statistics for biologists](#) contains articles on many of the points above.

Software and code

Policy information about [availability of computer code](#)

Data collection Zeiss Zen Blue acquisition software, Bio-Rad CFX Manager software, HMS O2 high-performance cluster

Data analysis Fiji (vs2.1.0), GraphPad Prism (vs9.5.1), Imaris (v10), 10x Genomics Cell Ranger (vs 6.1.1), Seurat (vs4.3.0)

For manuscripts utilizing custom algorithms or software that are central to the research but not yet described in published literature, software must be made available to editors and reviewers. We strongly encourage code deposition in a community repository (e.g. GitHub). See the Nature Portfolio [guidelines for submitting code & software](#) for further information.

Data

Policy information about [availability of data](#)

All manuscripts must include a [data availability statement](#). This statement should provide the following information, where applicable:

- Accession codes, unique identifiers, or web links for publicly available datasets
- A description of any restrictions on data availability
- For clinical datasets or third party data, please ensure that the statement adheres to our [policy](#)

Raw data from main and Extended Data Figures are available in the Source Data files provided with this work. Reagents are available upon request. The snRNA-seq datasets generated in this work are publicly available in the Gene Expression Omnibus (GEO) databases under GSE218641 accession code. GSE218641: [https://www.ncbi.nlm.nih.gov/geo/query/acc.cgi?acc=GSE218641], snRNA-seq dataset of gut from Ore R females flies during Homeostasis and Recovery

Single-nuclei profiling data from this study can be found at https://www.flyrnai.org/tools/rna_seq_base/web/showProject/39/plot_coord=1/sample_id=all, to allow users to query the expression of any gene of interest. All other data are available in Figures, Ext. Data Figures and SI files (SI, SI figure, S. videos, S. Tables)

Research involving human participants, their data, or biological material

Policy information about studies with [human participants or human data](#). See also policy information about [sex, gender \(identity/presentation\), and sexual orientation](#) and [race, ethnicity and racism](#).

Reporting on sex and gender	n/a
Reporting on race, ethnicity, or other socially relevant groupings	n/a
Population characteristics	n/a
Recruitment	n/a
Ethics oversight	n/a

Note that full information on the approval of the study protocol must also be provided in the manuscript.

Field-specific reporting

Please select the one below that is the best fit for your research. If you are not sure, read the appropriate sections before making your selection.

☒ Life sciences ☐ Behavioural & social sciences ☐ Ecological, evolutionary & environmental sciences

For a reference copy of the document with all sections, see [nature.com/documents/nr-reporting-summary-flat.pdf](https://www.nature.com/documents/nr-reporting-summary-flat.pdf)

Life sciences study design

All studies must disclose on these points even when the disclosure is negative.

Sample size	No statistical method was used to determine sample size. For mitotic division counts, RT-qPCR experiments, fluorescent intensity, cell ratio counts, ion balance, GCAMP imaging sample size was based on previous studies (PMID: 21098564, PMID: 28561738, PMID: 29414942, PMID: 30404917, PMID: 30650359, PMID: 32345720).
Data exclusions	No data were excluded
Replication	Each experiment was replicated 2-3 times
Randomization	Randomization was not applicable. Samples were allocated on control and experimental groups based on genotypes
Blinding	Blinded experiments were performed when counting mitotic divisions. For other experiments the investigators set up the experiments and analyzed the data making it impossible to perform blind analysis.

Behavioural & social sciences study design

All studies must disclose on these points even when the disclosure is negative.

Study description	n/a
Research sample	n/a
Sampling strategy	n/a
Data collection	n/a
Timing	n/a
Data exclusions	n/a
Non-participation	n/a

Randomization

n/a

Ecological, evolutionary & environmental sciences study design

All studies must disclose on these points even when the disclosure is negative.

Study description

n/a

Research sample

n/a

Sampling strategy

n/a

Data collection

n/a

Timing and spatial scale

n/a

Data exclusions

n/a

Reproducibility

n/a

Randomization

n/a

Blinding

n/a

Did the study involve field work?

☐ Yes☒ No

Reporting for specific materials, systems and methods

We require information from authors about some types of materials, experimental systems and methods used in many studies. Here, indicate whether each material, system or method listed is relevant to your study. If you are not sure if a list item applies to your research, read the appropriate section before selecting a response.

Materials & experimental systems

- n/a Involved in the study
- ☒ ☐ Antibodies
 - ☒ ☐ Eukaryotic cell lines
 - ☒ ☐ Palaeontology and archaeology
 - ☐ ☒ Animals and other organisms
 - ☒ ☐ Clinical data
 - ☒ ☐ Dual use research of concern
 - ☒ ☐ Plants

Methods

- n/a Involved in the study
- ☒ ☐ ChIP-seq
 - ☐ ☒ Flow cytometry
 - ☒ ☐ MRI-based neuroimaging

Antibodies

Antibodies used

Primary antibodies: rabbit anti-Flag (Sigma, F7425; 1:100), mouse anti- β -galactosidase (Promega Z378A; 1:500), rabbit anti-pH3 (Millipore #06-570; 1:3000), mouse anti-GFP (Invitrogen A11120; 1:500), mouse anti-ChAT (DSHB; 1:50), rabbit anti-GFP (Invitrogen A6455; 1:3000), rabbit anti-DsRED (Clontech #632496; 1:200), chicken anti-GFP (AVES 1020; 1:2000), rat anti-HA (Sigma 3F10; 1:500), mouse anti-Pros (DSHB MR1A; 1:50), rabbit anti-Syt1 (gift from Hugo Bellen; 1:1500), rabbit cleaved anti-Dcp1 (Cell Signaling Asp216; 1:100), rabbit anti-pdm1 (gift from Xiaohang Yang; 1:500), mouse anti-pdm1 (DSHB 2D4; 1:20), guinea pig anti-inx2 (gift from Guy Tanentzapf; 1:1000)

Phalloidin Alexa-647 (Invitrogen A2284; 1:50), Phalloidin Alexa-633 (Invitrogen A2287; 1:50), Phalloidin Alexa-405 (Invitrogen A30104; 1:50), DAPI (1:3000), Alexa Fluor-conjugated donkey-anti-mouse (ThermoFisher 1:1000, A-21202, A-31570, A-31571), donkey-anti-rabbit (ThermoFisher 1:1000, A-21206, A-31572), goat-anti-chicken (ThermoFisher 1:1000, A-78948), goat-anti-guinea pig (ThermoFisher 1:1000, A-21435) and donkey-anti-rat secondary antibody (ThermoFisher 1:1000, A-48270).

Validation

Validation of commercially available primary antibodies:

anti-Flag (Sigma, F7425) : <https://www.sigmaaldrich.com/US/en/product/sigma/f7425>

anti- β -galactosidase (Promega Z378A) : https://www.promega.com/products/protein-detection/primary-and-secondary-antibodies/anti_beta_galactosidase-mab/?catNum=Z3781

anti-pH3 (Millipore #06-570): <https://www.sigmaaldrich.com/US/en/product/mm/06570>

anti-GFP (Invitrogen A11120): <https://www.thermofisher.com/antibody/product/GFP-Antibody-clone-3E6-Monoclonal/A-11120>

anti-ChAT (DSHB; 1:50): <https://dshb.biology.uiowa.edu/ChAT4B1>

anti-GFP (Invitrogen A6455): <https://www.thermofisher.com/antibody/product/GFP-Antibody-Polyclonal/A-6455>

anti-DsRED (Clontech #632496; 1:200): <https://www.takarabio.com/products/antibodies-and-elisa/fluorescent-protein-antibodies/red-fluorescent-protein-antibodies>
 anti-GFP (AVES; 1020): <https://www.aveslabs.com/products/anti-green-fluorescent-protein-antibody-gfp>
 anti-HA (Sigma 3F10): <https://www.sigmaaldrich.com/US/en/product/roche/12158167001>
 anti-Pros (DSHB MR1A): <https://dshb.biology.uiowa.edu/Prospero-MR1A>
 anti-pdm1 (DSHB 2D4): <https://dshb.biology.uiowa.edu/Nub-2D4>
 anti-Dcp1 (Cell Signaling Asp216): <https://www.biocompare.com/9776-Antibodies/3247906-Cleaved-Drosophila-Dcp-1-Asp216-Antibody/>

For non-commercial primary antibodies the information is in the following relevant publications:

anti-Syt1, PMID: 8269841

anti-pdm1, PMID: 21078993, PMID: 21098564

anti-inx2, PMID: 26116660

Animals and other research organisms

Policy information about [studies involving animals](#); [ARRIVE guidelines](#) recommended for reporting animal research, and [Sex and Gender in Research](#)

Laboratory animals

Drosophila melanogaster.

Publicly available flies:

mex1-Gal4, mex1-Gal4 Tubulin-Gal80TS, mex1-Gal4 UAS-2x-GFP, esg-sfGFP, ChATMI04508-Gal80, Tsh-Gal80, R49E06-Gal4 (BDSC:38689), Tubulin-Gal80TS; R49E06-Gal4, VT004958-p65AD (BDSC: 71993), VT047163-Gal4DBD (BDSC: 75312), VT004958-p65AD;VT047163-Gal4DBD, hml-Gal4 UAS-GFP (BDSC: 30142), Tubulin-Gal80TS (BDSC:7018,7019) Myo1A-Gal4, myo1A-Gal4 UAS-GFP, Myo1A-Gal4 Tubulin-Gal80TS, esg-Gal4 Tubulin-Gal80TS, Tubulin-Gal80TS; esg-Gal4, esg-Gal4, Su(H)GBE-Gal4 UAS-CD8-GFP; Tubulin-Gal80TS, Tubulin-Gal80TS; pros-Gal4, elav-Gal4; Tubulin-Gal80TS, Tubulin-Gal80TS ; how24B-Gal4, upd3-Gal4 UAS-GFP, 20XUAS-IVS-jGCaMP7c (BDSC: 79030)57, TOE.GS01624 (BDSC: 79471)58, UAS-3XFLAG-dCas9-VPR (BDSC: 66562), UAS-nAChRbeta3RNAi (BDSC: 25927)59, UAS-2x-GFP (BDSC: 6874), LexAop-CD8-GFP-2A-CD8GFP;UAS-mLexA-VP16-NFAT LexAop-rCD2-GFP (BDSC:66542)60, UAS-Orai, UAS-ChATRNAi (BDSC:25856)59, UAS-scRNAi (BDSC: 26206), 20XUAS-6XGFP (BDSC: 52262), 10XUAS-mCD8::GFP (BDSC:32184, 32186), UAS-mCD8::GFP QUAS-mtdTomato-3xHA (BDSC:30118), QUAS-mtdTomato-3xHA (BDSC: 30005), 20XUAS-6xGFP (BDSC: 52262), 20XUAS-6xmCherry-HA (BDSC: 52268), 5xUAS-IVS-Syt1::smGdP-HA (BDSC:62142), 10xUAS-IVS-myr::GFP (BDSC: 32198), 13xLexAop2-6xGFP (BDSC: 52265)63, UAS-shibireTS (BDSC: 44222)64, UAS-CsChrimson (20XUAS-IVS-CsChrimson.mCherry, BDSC: 82181), QUAS-CsChrimson, 13xLexAop-sfGFP, UAS-TrpA1, UAS-wgnRNAi (BDSC: 55275), UAS-wgnRNAi-2 (BDSC: 50594), UAS-grndRNAi (GD12580/v43454), UAS-Inx2RNAi (BDSC: 29306), UAS-Inx7RNAi (BDSC:26297), UAS-eigerIR (BDSC: 58993), UAS-DenMark (BDSC:33061)68, lexAop-UAS-morphotrap.ext.mCh (BDSC:68171), 13xLexAop-IVS-jGCaMP7c (BDSC:80916), 4xUAS-PV-Myc (BDSC:25030)70, UAS-emptyVVK37, UAS- LuciferaseRNAi (BDSC: 31603), UAS-Luciferase (BDSC: 35789). Egr-GFP (BDSC: 66381),Diap1-LacZ (BDSC:12093), Vn-LacZ (BDSC:11749), Ex-LacZ (BDSC: 44248).

Flies generated in this study:

UAS-nAChRbeta3RNAi-2, UAS-nAChRbeta3, LexAop-nAChRbeta3, Mex1-LexA::GAD, nAChRbeta3-flag

Wild animals

the study did not involve wild animals

Reporting on sex

Females, 3-5 days old

Field-collected samples

not applicable

Ethics oversight

No ethical approval was required

Note that full information on the approval of the study protocol must also be provided in the manuscript.

Flow Cytometry

Plots

Confirm that:

- ☒ The axis labels state the marker and fluorochrome used (e.g. CD4-FITC).
- ☒ The axis scales are clearly visible. Include numbers along axes only for bottom left plot of group (a 'group' is an analysis of identical markers).
- ☒ All plots are contour plots with outliers or pseudocolor plots.
- ☒ A numerical value for number of cells or percentage (with statistics) is provided.

Methodology

Sample preparation

For homeostasis 3-5 days old Ore R female flies were fed standard lab food at 29°C for 6 days. For recovery d2 3-5 days old Ore R female flies were fed 2%DSS for 4 days at 29°C and then transferred to standard food at 29°C for 2 days. 70 guts per condition were dissected in cold Schneider's medium, flash-frozen and stored at -80°C. Prior to FACs sorting, samples were spined down and Schneider's medium was exchanged with homogenization buffer [250mM Sucrose, 10mM Tris pH8, 25mM KCl, 5mM MgCl, 0.1% Triton-X, 0.5% RNasin Plus, 50x protease inhibitor, 0.1mM DTT]. Using 1ml dounce, nuclei were released by 20 loose pestle strokes and 40 tight pestle strokes while keeping samples on ice and avoiding foam. Next, nuclei were filtered through 5 ml cell strainer (40 µm), and using 40 µm Flowmi. Nuclei were centrifuged, resuspended in PBS/0.5%

	BSA with 0.5% RNase inhibitor, filtered again with 40 µm Flowmi and stained with DRAQ7™ Dye.
Instrument	Sony SH800Z Cell Sorter
Software	Sony software
Cell population abundance	100k nuclei per sample (n=70 guts per sample) were collected in PBS/BSA buffer.
Gating strategy	Nuclei were stained with fluorescent DNA dye DRAQ7. The gating strategy to collect gut nuclei per sample is shown in SI Fig.1. Multiple nuclei populations were detected in both samples which is indicative of polyploid gut cells. These were the populations that were selected.

☒ Tick this box to confirm that a figure exemplifying the gating strategy is provided in the Supplementary Information.